University of California
Santa Barbara

Simulations of open ballistic quantum systems and semiclassical semiconductor superlattices

A dissertation submitted in partial satisfaction
of the requirements for the degree

Doctor of Philosophy
in
Physics

by

Jonathan Essen

Committee in charge:

Professor Mark Sherwin, Chair
Professor Chetan Nayak
Professor Mark Srednicki
Professor Björn Birnir, Co-Chair

September 2017

The Dissertation of Jonathan Essen is approved.

Professor Chetan Nayak

Professor Mark Srednicki

Professor Björn Birnir, Co-Chair

Professor Mark Sherwin, Committee Chair

June 2017

Simulations of open ballistic quantum systems and semiclassical semiconductor superlattices

Jonathan Essen

Acknowledgements

Looking back on my time here at UC Santa Barbara, it's tempting to recall an idyllic experience, bathed in a rosy-golden sunset glow: I met some rather interesting classmates, I learned to surf, I interacted with some of the best physicists and mathematicians in the world, and I even contributed a few ideas of my own. Nonetheless, I must admit that the last ten years have been incredibly difficult for me. I never could have made it this far if not for the support of my parents, my wife Ellie, my brothers, my friends, and my advisors.

I am not quite sure how or why I latched onto the idea of doing physics. I suppose that I just kept wondering how things work. During college, I saw Martin Lo speak at Jet Propulsion Laboratory and I made up my mind to work with him. I found my opportunity through UCLA's Institute for Pure and Applied Mathematics. I met Ellie around this time and learned that she was starting graduate school in mathematics at UCSB. I made up my mind to study physics at UCSB, and so it all began.

During my first year here, I was shocked by the level of intensity, which was beyond anything I had ever encountered. In my second year, I began studying under Chetan Nayak, who introduced me to the two-dimensional electron gas. I attempted to calculate the effects of subband-mixing in the quantum Hall problem. However, I came to realize that I wasn't quite ready for this problem, and I had to admit defeat. After a year spent looking for another thesis project, I found myself taking the oral exam for a terminal Masters degree. I left the department and decided to focus on surfing for a while. One day, I decided to approach Björn Birnir of the mathematics department. To my surprise, he acted as though I had never left the physics department, and re-introduced me to Mark Sherwin (I had been a TA for Mark during my first year at UCSB). Mark proposed a thesis project that I thought I could manage: A subband-mixing problem without

the pesky magnetic field! I was re-admitted to the physics department, but by this time, I had moved to Malibu with Ellie, who was teaching mathematics at Pepperdine University. Björn The commute between Malibu and Santa Barbara was quite pretty, but also exhausting. Laurel Smith, a friend of my parents' friend, let me stay in her guest room for a couple of nights per week. I advanced to candidacy, and Björn invited Ellie and me to visit the University of Reykjavik in Iceland. There we met Luis Bonilla, who helped me to better understand the Wigner function. Our discussions inspired me to persue the idea of open boundary conditions for quantum systems.

Ellie and I moved back to Santa Barbara after we were married. I began working out of Mark Sherwin's lab, where I met Nutan Gautam, Brian Youngblood, Hunter Banks, Blake Wilson, Darren Valovcin, Jessica Banks, and Changyun Yoo. I found the energy and inclusive culture of this research group to be incredibly refreshing, and this energy propelled me forward in the subband-mixing theory.

Many others helped me along the way: One of the first people I ever met at UCSB was Joe Polchinski. Even though I never worked closely with him, he and I talked many times over the years, and our conversations meant the world to me. Idse Heemskerk, my officemate during my first year of graduate school, taught me how to get physics done. Erik Perkins has been another great source of inspiration to me over the years. Ian Jenkins has been a great friend and collaborator on the superlattice theory.

I am undeniably blessed to be supported by such a group of people! Thank you!

To Mom, Dad, and Ellie

Curriculum Vitæ

Jonathan Essen

Education

2017	Ph.D. in Physics, University of California, Santa Barbara.
2011	M.A. in Physics, University of California, Santa Barbara.
2006	B.S. in Physics and Mathematics, Principia College, Elsah, Illinois.

Publications

M. Ruiz-Garcia, J. Essen, M. Carretero, L. L. Bonilla, and B. Birnir, "Enhancing chaotic behavior at room temperature in GaAs/(Al,Ga)As superlattices" Phys. Rev. B 95, 085204

J. Essen, M. Ruiz-Garcia, I. Jenkins, M. Carretero, L. L. Bonilla, and B. Birnir, "High-frequency parameter dependence of nonlinear dynamical phenomena in GaAs/(Al,Ga)As superlattices" (submitted)

J. Essen, "Perfectly matched layers for the Liouville-von Neumann equation" (in preparation)

Abstract

Simulations of open ballistic quantum systems and semiclassical semiconductor superlattices

by

Jonathan Essen

The tunable antenna-coupled intersubband terahertz (TACIT) sensor is a heterodyne mixer based on the coupling of intersubband absorption with the sheet resistivity of doped GaAs/AlGaAs quantum wells. A theoretical treatment of this device as an open quantum system operating at the ballistic limit leads to the development of perfectly matched layers for the position-space Liouville-von Neumann equation.

Meanwhile, the nonlinear dynamics of weakly-coupled, doped GaAs/AlGaAs superlattices in the sequential-tunneling regime are theoretically characterized by computing the Poincaré map of a self-consistent, semiclassical resonant tunneling model. Applied to shorter superlattices at higher bias voltages, period-doubling cascades to high-frequency chaos are observed, and their robustness to variations in the design parameters is explored.

Contents

Chapter 1

The TACIT sensor: Coupling in-plane and inter-subband dynamics

This work is motivated in part by the need to further the basic understanding the *tunable antenna-coupled intersubband terahertz* (TACIT) sensor, which has been iteratively developed under Mark Sherwin at the Institute for Terahertz Science and Technology (ITST) at UC Santa Barbara since the 1990s. This device promises to increase the sensitivity and improve the operable temperature range of far-infrared sensors, which are sensitive to electromagnetic fields at frequencies of a few terahertz (THz). An interesting feature of the TACIT sensor is that it couples the motion of electrons between two very different realms. In one realm, their motion is described by a two-state quantum system. In the other realm, their motion takes place along two continuous spatial coordinates.

The physical system responsible for this strange combination is called a *quantum well*. Quantum wells are semiconductor heterostructures consisting of three layers — a thin layer of Aluminum Gallium Arsenide (AlGaAs), sandwiched between two much thicker layers of Gallium Arsenide (GaAs). Depending on the Aluminum concentration, the conduction band of AlGaAs can be made hundreds of meV lower than that of GaAs,

so that conduction band of the heterostructure contains a narrow channel, or "well." The conduction band of the thin sheet of AlGaAs is broken up into quantized *subbands*, where each subband corresponds to a bound state of the confinement potential. For sufficiently narrow wells at sufficiently low temperatures, the intersubband energy spacing becomes large compared to the Boltzmann energy $k_B T$.

The TACIT sensor relies on coupling a large population of electrons to the electromagnetic field in order to meet its design objectives. The collective dynamics of these electrons contain nonlinear feedback mechanisms due to their mutual repulsion via the Coulomb interaction. The electron-electron interaction in the TACIT sensor significantly modifies the shape of the confinement potential. The stationary self-consistent solution of the Schrödinger-Poisson equation for a uniform, 40 nm quantum well with sheet density $N_s = 1.5 \times 10^{11}/\text{cm}^2$ is shown in Figure 1.1.

The TACIT sensor is populated with electrons by a process called *remote delta doping*: Silicon (Si) atoms, which are electron donors, are deposited over a thin sheet within the GaAs layers of the heterostructure, near to the AlGaAs well. Many of the donated electrons diffuse to the bottom of the well once the system has reached thermal equilibrium. At the relevant doping densities and sufficiently low temperatures, the trapped electrons mainly occupy the lowest subband. The resulting system of electrons is called a *two-dimensional electron gas* (2DEG). The electrons behave like free, i.e. *ballistic* quantum particles propagating two dimensions. The 2DEG can also oscillate into the third dimension by undergoing *intersubband transitions*.

The TACIT sensor consists of a remotely-doped quantum well wafer with four electrical contacts, as shown in Figure 1.2. The *source* and *drain* are designed to make Ohmic contact with the 2DEG, allowing a two-dimensional sheet of current to flow between them. The metallic *top* and *back gates* are deposited on opposite sides of the wafer, and they are responsible for locally bending and tilting the quantum well. The top and back

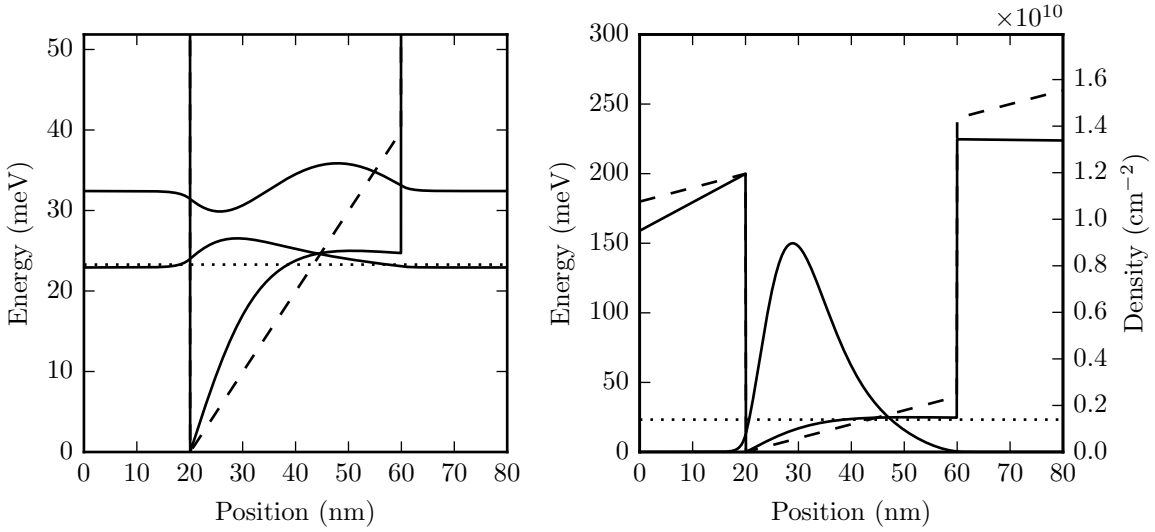

Figure 1.1: The self-consistent solution of a remotely-doped, 40nm, 200meV quantum well at 30K under a uniform electric field of $1\text{mV}\,\text{nm}^{-1}$ with a sheet density of $1.5 \times 10^{11}\text{cm}^{-2}$. (Left) the envelope wavefunctions of the lowest two subbands and the self-consistent confinement potential (solid lines). (Right) the sheet density profile and the self-consistent confinement potential (solid lines). In both images, the bare confinement potential (dashed line), and the chemical potential (dotted line) are also visible.

gates may also drive intersubband transitions if their voltages oscillate relative to one another at frequencies near the intersubband resonance. The intersubband resonance is tunable over a wide frequency range (a few THz) by varying the average voltage between the top and back gates. The area between the top and back gates is called the *active region*. Assuming that the intersubband excitations due to the absorption of THz radiation are rapidly thermalized within the active region, they cause the 2DEG to become warmer, which reduces the source-drain conductivity. Hence the frequency and intensity of the THz radiation may be detected by measuring the source-drain conductivity [1].

The description outlined above provides an intuitively appealing explanation of the operation of the TACIT sensor, but in the extremely clean quantum wells available today, the TACIT sensor may operate closer to the *ballistic limit*, and it is important to gain

a better understanding of this limit in order to improve on the design of the sensor. A theoretical description of the TACIT sensor in the ballistic limit needs to account for transport between the source and the drain coupled with intersubband transitions inside the active region. Additionally it needs to account for the collective nature of the response of the 2DEG to the localized, *vertically*-polarized fields (between the top and back gates) inside the active region, as well as the *horizontally*-polarized fields (between the source and drain) at the edges of the active region. The first goal of this thesis is to lay out the ballistic theory of the TACIT sensor and to develop computational methods for its simulation. Of course, thermalization processes are also very important to the physics of the TACIT sensor, therefore the theory under development here has been designed to be amenable to the inclusion these effects.

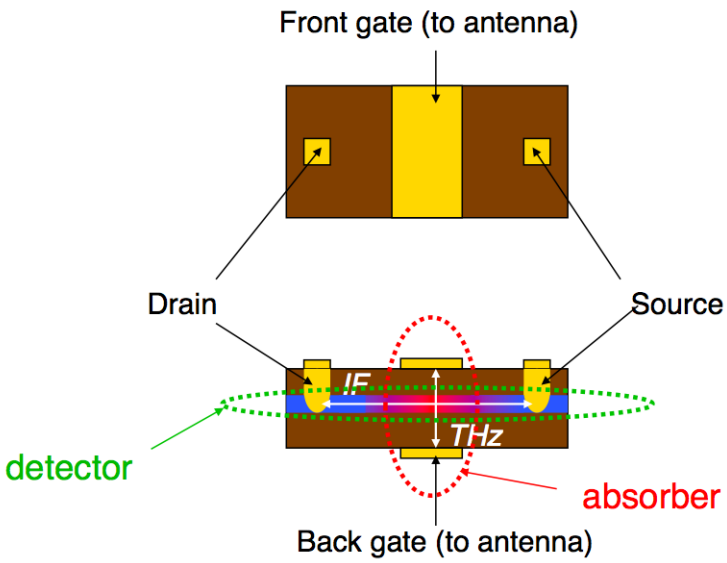

Figure 1.2: Schematic diagram of the TACIT sensor.

In order to simulate the collective response of the 2DEG to the electromagnetic field, it is necessary to define a *computational box* surrounding the active region, in which the simulations of this theory are to be carried out. However, the complete set of electronic wavefunctions for this system live on a much larger domain. The electronic density is

given by the diagonal elements of the position-space density matrix, which involves a sum over the complete set of wavefunctions. It is necessary to match the evolution of the density matrix over the interior of the computational box with the exact evolution over the larger domain. This implies that the edges of the computational box must be transparent to any fluctuations propagating outwards from its interior. Hence we seek a numerical method capable of absorbing the outgoing fluctuations at the edges of the box without inducing artificial reflections.

The approach taken here is to develop *perfectly matched layers* (PMLs) for the position-space Liouville-von Neumann equation. Some motivation and a review of PMLs for the Schrödinger equation are reviewed in Chapter 2. An original numerical method for the time-evolution of the density matrix in position space with perfectly matched layers is given in Chapter 3. This numerical method scales with computational complexity of $O(N_x^2 \log N_x)$, where N_x is the discrete position space of the computational domain. The numerical method accurately captures the time evolution of pure quantum states, and hence the ballistic limit. It is also naturally parallelizable and lends itself to efficient implementation in distributed computing environments or on specialized hardware.

The purpose of this chapter is to provide a description of the TACIT sensor in the ballistic limit, paying special attention to the complete set of basis wavefunctions. First, the geometry of the conducting channel is laid out. Since the source and drain contacts are tens of microns away from the active region, which is only about 5 square microns in area, the active region will be treated as if the source and drain were infinitely far away. Next, the three-dimensional stationary Schrödinger equation is expressed as a set of coupled one-dimensional Schrödinger equations, one for each subband. The solution of the stationary, subband-mixing Schrödinger equation gives a complete basis of transmission-reflection states, and this is used to outline a first-order linear response theory using the Born approximation.

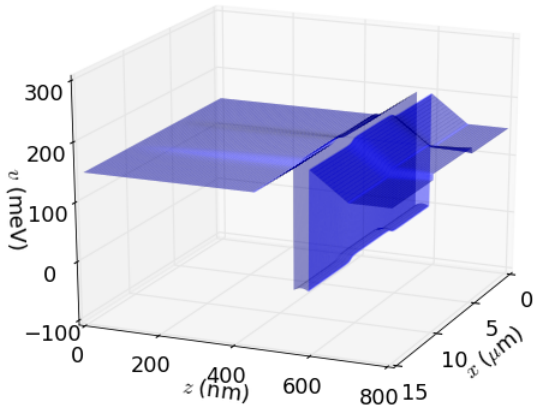

Figure 1.3: The shape of the conducting channel. The top- and back-gates are placed at $z = 0$nm and $z = 800$nm, spanning the interval $5 \leq x \leq 10$µm. The donors are deposited at $z = 450$nm and $z = 690$nm. The back gate voltage is chosen to coincide with the conduction band energy. The top gate voltage is chosen to be 50mV above the conduction band.

1.1 Geometry of the TACIT sensor

The quantum well making up the TACIT sensor is treated as though it spans an infinite length in the x-direction and has a width of 5µm in the y-direction. The x-direction points from the source to the drain, the y-direction points transverse to the x-direction, and the z-direction points in the normal direction to the quantum well, aka the growth direction. The shape of the conduction band, projected into the x-z plane, is sketched in Figure 1.3. The channel is taken to be completely flat in the y-direction. It is also taken to be flat in the x-direction, outside of the active region. The top and back gates modify the shape of the well as follows: Simultaneously increasing the voltages of the top and back gates raises the bottom of the well, developing a potential barrier. The difference between the top and back gate voltages affects the slope of the active region along the z-direction.

The metallic plates forming top and back gates are square-shaped and have an area of about 5µm^2. In the real TACIT sensor, the electromagnetic field propagates down the y-direction and this may create some inhomogeneities in the response of the 2DEG along the y-direction. However, since the electromagnetic modes of the waveguide coupling the device to the antenna are not being treated in this work, the TACIT is treated as though it remains homogeneous along the y-direction. This allows for the y-direction to be integrated out and the system to be reduced to a set of coupled one-dimensional problems.

1.2 Separation of variables

The stationary Schrödinger equation in 3d is solved in this section. The result is an eigenvalue problem which gives a complete set of states. Focusing our attention to the electrons occupying the bottom of the well, the Schrödinger equation is

$$\left\{\frac{-\hbar^2}{2m}(\partial_x^2+\partial_y^2+\partial_z^2)+v_{3\mathrm{d}}(x,y,z)\right\}\psi_{3\mathrm{d}}(x,y,z)=\varepsilon\psi_{3\mathrm{d}}(x,y,z), \tag{1.1}$$

where $v_{3\mathrm{d}}(x,y,z) = u(x,z) + w(y)$ and ε is the total energy. The function $u(x,z)$ is similar in shape to the potential energy surface shown in Figure 1.3 and $m = m_e/15$ is the electron's effective mass in GaAs. The function $w(y)$ is taken to be an infinitely-deep well of width $L_y = 5$µm. The y-dependence is separated out as follows. First, put

$$\psi_{3\mathrm{d}}(x,y,z)=\phi(x,z)\chi_\ell(y) \tag{1.2}$$

where

$$\chi_\ell(y) = \sqrt{\frac{2}{L_y}} \sin \frac{\ell \pi y}{L_y} \tag{1.3}$$

Then equation (1.1) reduces to

$$\left\{ \frac{-\hbar^2}{2m}(\partial_x^2 + \partial_z^2) + u(x,z) \right\} \phi(x,z) = \varepsilon_x \phi(x,z) \tag{1.4}$$

where $\varepsilon = \varepsilon_x + \varepsilon_y^\ell$ and $\varepsilon_y^\ell = \hbar^2 \ell^2 \pi^2 / 2mL_y^2$. Next, put

$$\phi(x,z) = \psi(x)\xi_n(x,z) \tag{1.5}$$

where

$$\left\{ \frac{-\hbar^2}{2m}\partial_z^2 + u(x,z) \right\} \xi_n(x,z) = \varepsilon_z^n(x)\xi_n(x,z) \tag{1.6}$$

The equation above is solved by fixing x to some particular value and then solving the resulting 1d eigenvalue problem along the z-direction. The solutions are the *local envelope wavefunctions* $\xi_n(x,z)$ with the eigenvalues $\varepsilon_z^n(x)$, where $\varepsilon_z^n(x)$ is the excitation of subband n above $v(x)$, defined to be the minimum of $u(x,z)$ along the x-slice of interest, ie. the bottom of the channel

$$v(x) = \min_z u(x,z). \tag{1.7}$$

The TACIT sensor consists of 40nm quantum wells with doping densities near 1.5×10^{11} cm^{-2}. At low temperatures, only the lowest two subbands are significantly occupied, even under strong driving fields near the intersubband resonance. In principle, any number of

bound states could be included. Expanding the z-dependence of $\phi(x,z)$ in the basis of local envelope wavefunctions, we have

$$\phi(x,z) = \sum_n \psi_n(x)\xi_n(x,z), \tag{1.8}$$

where $\psi_n(x)$ describes the x-dependence of an electronic state associated with the nth subband. Then equation (1.4) reduces to

$$\sum_n \left\{ \frac{-\hbar^2}{2m}\partial_x^2 + v(x) + \varepsilon_z^n(x) \right\} \psi_n(x)\xi_n(x,z) = \varepsilon_x \sum_n \psi_n(x)\xi_n(x,z) \tag{1.9}$$

Equation (1.9) is multiplied on both sides by $\xi_{n'}(x,z)$ and then integrated on both sides with respect to z. Making use of the orthogonality of the $\xi_n(x,z)$, this gives

$$\sum_{n'} \left\{ -\frac{\hbar^2}{2m}\Big[\delta_{nn'}\partial_x^2 + 2w_{nn'}(x)\partial_x + u_{nn'}(x)\Big] + \delta_{nn'}\Big[v(x) + \varepsilon_z^n(x)\Big] \right\} \psi^{n'}(x) = \varepsilon_x^n \psi_n(x) \tag{1.10}$$

where

$$w_{nn'}(x) = \int dz \xi_n^*(x,z)\partial_x \xi_{n'}(x,z) \tag{1.11}$$

$$u_{nn'}(x) = \int dz \xi_n^*(x,z)\partial_x^2 \xi_{n'}(x,z) \tag{1.12}$$

The local envelope energy $\varepsilon_z^n(x)$ appears as an effective potential term describing the height of the barrier induced by the voltages of the top and back gates. This effect is called *subband bending*. The off-diagonal terms $w_{nn'}(x)$ and $u_{nn'}(x)$ reveal that it is possible for an ingoing electron in a given subband to develop a non-zero amplitude in another subband. This effect is called *subband mixing*.

1.2.1 Transmission-reflection states

In the rest of this work, we will assume that equation (1.10) does not support any bound states. This is equivalent to the statement that all states are unbound in the x-direction. Hence a complete basis of states is given by the solutions of the transmission-reflection problem, which have a *continuous* energy spectrum (even after discretizing the x-axis). The basis of transmission-reflection states is described as follows: The reservoirs on the left and right sides of the active region supply a complete set of *ingoing states*. The ingoing states are right- and left-moving eigenstates associated with the left and right reservoirs respectively. The reservoirs are taken to be infinite, x-invariant channels of identical geometry, which smoothly match with the active region at the edges of the computational domain x_L and x_R. The envelope wavefunctions associated with the reservoirs are the x-independent eigenfunctions $\xi_n(z)$ with energies E_z^n. Since the reservoirs are invariant in x, the Schrödinger equation describing the ingoing states does not contain any subband mixing terms. Consequently the ingoing states are the plane wave states

$$\langle \vec{x}|k\ell n\sigma\rangle_{\text{in}} = e^{i\sigma k(x-x^{\text{in}})} e^{i\pi\ell y/L_y} \xi_n(z) \tag{1.13}$$

where $\sigma = \pm 1$ signifies whether the ingoing state is associated with the left $(+)$ or right $(-)$ reservoir and $x^{\text{in}} = x_{L,R}$ respectively. The total eigen-energy of the state $|k\ell n\sigma\rangle_{\text{in}}$ is $E_{k\ell n\sigma} = E_x^{k\sigma} + E_y^\ell + E_z^n$, where $E_x^{k\sigma} = \hbar^2 k^2/2m$ and $E_y^\ell = \hbar^2\pi^2\ell^2/2mL_y^2$. At the interfaces between the reservoir and the active region, we have $(E_x^{k\sigma} + E_z^n) \to \varepsilon_x^n$ and $E_z^n \to \varepsilon_z^n(x^{in})$. (We already have $E_y^\ell = \varepsilon_y^\ell$.)

It is necessary to compute transmission-reflection states numerically. This can be accomplished by generalizing the one-dimensional numerical method due to Arnold [2] in order to account for subband mixing terms. Some details of the numerical implementation

are given in Appendix A. The basic idea is to choose the the ingoing state $|k, \ell, n, \sigma\rangle_{\text{in}}$ and then solve the discrete form of equation (1.10) for the stationary wavefunction. In order to account for the top and back gate voltages, the solution of the two-dimensional Poisson equation must be obtained numerically. The numerical solution of Poisson's equation is discussed in Appendix B. Figure 1.3 was created from this numerical method.

An interesting effect of the mixing terms can be seen in Figure 1.4: In the top row, an ingoing transmission-reflection state originating in the lowest subband (blue line) approaching from the left side was chosen to have enough total energy (dashed line) to make it over the potential barrier created by the gates, but not enough energy to (classically) occupy the second subband. The middle row of Figure 1.4 shows the mixing terms in dimensionless units. We can see that they are only nonzero near the edges of the active region, where the fields of the top and back gates twist the shape the well, causing it to tilt in the z-direction. The bottom row of Figure 1.4 shows the real part of the transmission-reflection wavefunction projected onto the two lowest subbands. We can see that the first-excited subband develops a nonzero amplitude where the mixing terms are strongest. Since this electronic state not classically allowed to occupy the first-excited subband, this behavior can be interpreted as a virtual transition.

The transmission-reflection states can be used to form the local density of states (LDOS)

$$\rho^n_{\text{loc}}(E(k), x) = |\psi_{kn}(x)|^2 \tag{1.14}$$

where $E(k) = \hbar^2 k^2 / 2m$. The LDOS for ingoing reservoir states in the lowest subband is shown in Figure 1.5. It can be observed that the LDOS is peaked near the leading of the active region, as viewed from the reservoir. The LDOS is also somewhat larger inside the active region, provided the ingoing states have enough energy to make it over the

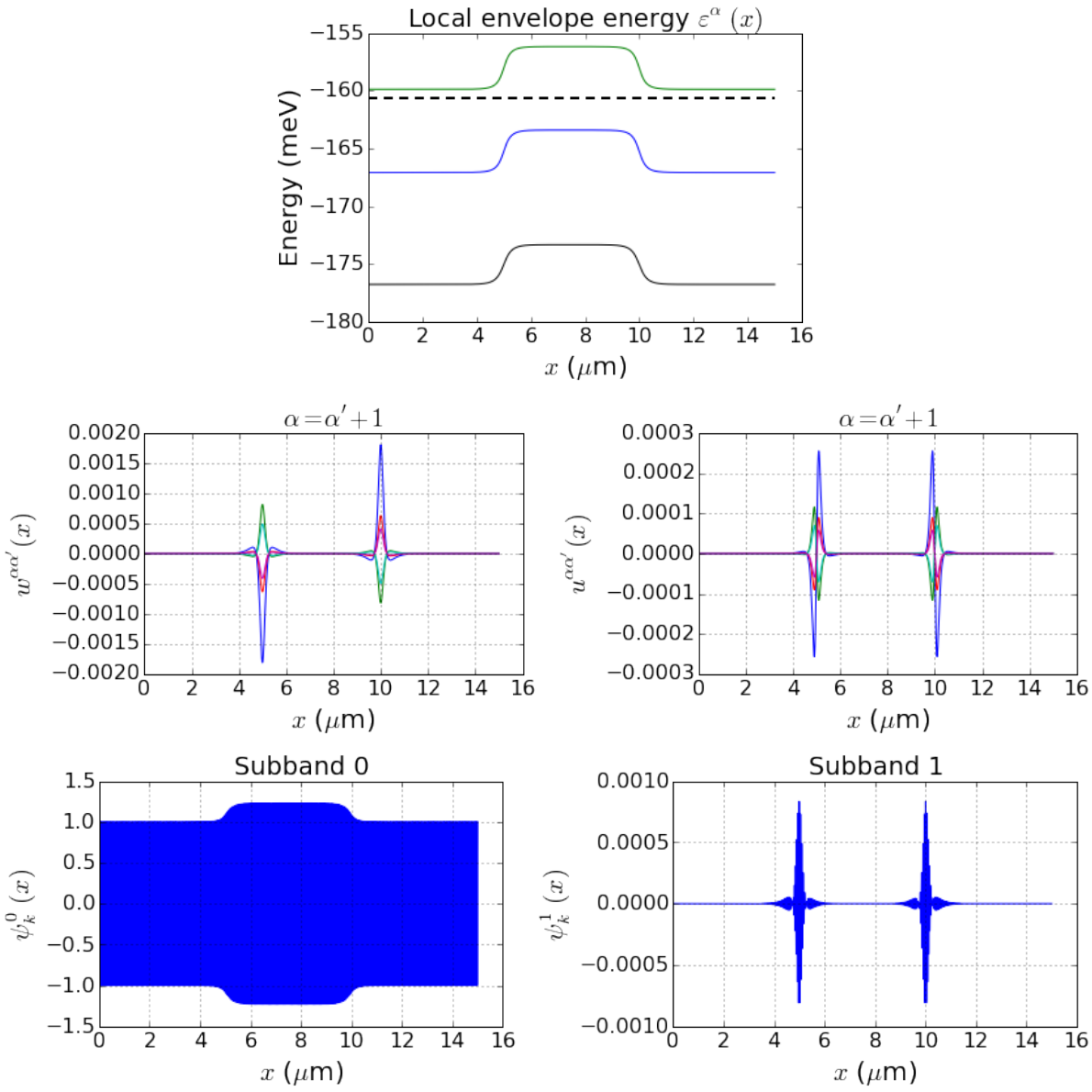

Figure 1.4: The top panel shows the bottom of the channel $v(x)$ in black and $v(x) + \varepsilon_z^n(x)$ for the lowest two values of n in blue and green. The dashed line represents the energy of a state incoming from the left side into the lowest subband (blue line). The middle row shows the mixing terms $w^{nn'}(x)$ and $u^{nn'}(x)$. The $0 \to 1$ mixing terms are shown in blue and have the largest magnitude. The bottom row shows the real parts of the transmission-reflection wavefunction.

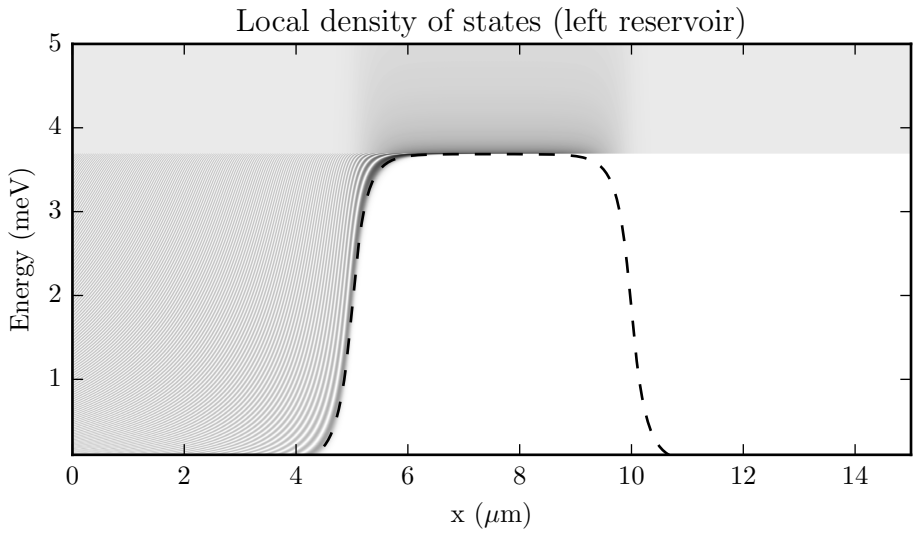

Figure 1.5: The local density of states for ingoing states of the left reservoir in the lowest subband. Darker regions correspond to higher values of ρ_{loc}. The dashed line represents the local envelope energy of the lowest subband $\varepsilon_z^0(x)$.

potential barrier. This feature can be interpreted as follows: In the ballistic limit, the reflection amplitude for a potential barrier is the same as for a potential drop. Therefore the active region can behave as a weak trap, since an electron inside the active region approaching the edge has a significant probability of being reflected back inside.

1.3 Photoconductance

The formula for the first-order response of the 2DEG to the localized fields of the top and back gate is now derived using the Born approximation. The constituent matrix elements give some insight into *indirect* intersubband transitions that exchange momentum with oscillating fields of the top and back gate.

Since the confinement energy of the y-direction is extremely small compared with the Fermi energy, we may replace the discrete index ℓ with the continuous index $k_y = \ell\pi/L_y$, and relabel the basis kets as $|k_x k_y n\sigma\rangle$. It is sometimes convenient to label

the basis kets $|E_x E_y n\sigma\rangle$, where the dispersion relation in the y-direction matches with the continuum limit, $E_y = \hbar^2 k_y^2/2m$, and the dispersion relation in the x-direction is $E_x = \hbar^2(1-\cos(k_x h_x))/2mh_x^2$ due to the discretization of the x-axis, where h_x is the spacing of the numerical grid. In order to check against the analytic results for the infinite plane geometry below, it is necessary refine the x-grid until the $E_x(k_x)$ matches with the continuum limit (and also $E_y(k_y)$) over the energy range of the Fermi integrals. The dispersion relations are plotted in Figure 1.6. Choosing $h_x \sim 1$ nm there is almost no visible discrepancy over about 50 meV.

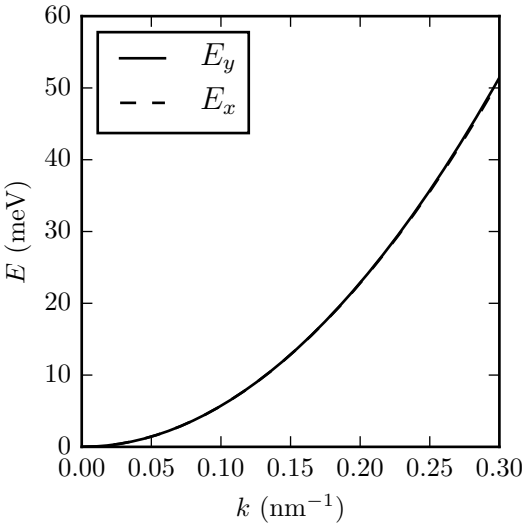

Figure 1.6: The E_x and E_y dispersion relations with $h_x = 0.916$nm.

The next tool needed is the Landauer formula. The current of a ballistic quantum system is written as [3]

$$J = \frac{2e}{h} \sum_{n\sigma} \int dE_x dE_y \; \sigma f_{n\sigma}(E_x, E_y) T_{n\sigma}(E_x, E_y) \tag{1.15}$$

where $f_{n\sigma}$ is the Fermi function

$$f_{n\sigma}(E_x, E_y) = \left[1 + e^{(E_x+E_y+E_z^n-\mu_\sigma)/k_BT}\right]^{-1}, \tag{1.16}$$

T is the temperature, and $T_{n\sigma}(E_x, E_y)$, sometimes written as $T_{k_xk_yn\sigma}$, is the total flux transmission probability

$$T_{k_xk_yn\sigma} = \sum_{n'} |k_x/k'_x| \, |t^{n'}_{k_x,k_y,n,\sigma}|^2 \tag{1.17}$$

where k'_x is the wavevector of the outgoing subband n' for the transmission-reflection state and $t^{n'}_{k_x,k_y,n,\sigma}$ is the transmission-reflection wavefunction evaluated at the outgoing edge.

Assuming there are no transitions between the y energy levels, the transmission function is independent of E_y, and we can perform the integral over E_y in the Landauer formula. We define the *thermal weights*

$$w_{n\sigma}(E_x) = \int dE_y f_{n\sigma}(E_x, E_y) \tag{1.18}$$

and write the current formula as

$$J = \frac{2e}{h} \sum_{n\sigma} \int dE_x \; \sigma w_{n\sigma}(E_x) T_{n\sigma}(E_x). \tag{1.19}$$

The thermal weights are formally equal to a polylogarithm function, but in practice, we represent $w_{n\sigma}$ using an interpolating function. It is sometimes useful to represent the thermal weights as a function of k_x instead of E_x. The accuracy of the interpolation can be checked by computing the sheet density of a single-subband 2DEG using the thermal

weights

$$N_s(\mu, T) = \frac{1}{\pi^2} \sum_{\sigma} \int_{-\infty}^{\infty} dk_x \, w_\sigma(E_x(k_x) - \mu), \tag{1.20}$$

and comparing the result against the exact result for the infinite plane geometry

$$N_s^{\infty}(\mu, T) = \frac{m k_B T}{\pi \hbar^2} \ln(1 + e^{\mu / k_B T}). \tag{1.21}$$

Sampling a sufficient number of points for the interpolating function representing the thermal weghts gives excellent agreement as shown in Figure 1.7.

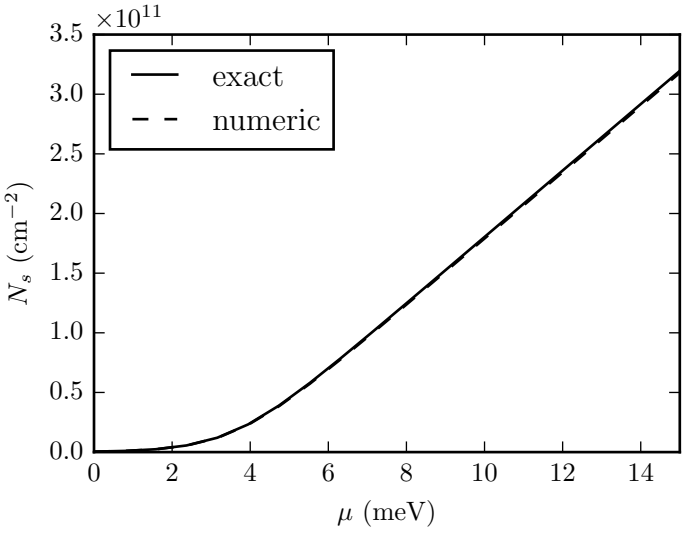

Figure 1.7: The sheet density of a single-subband 2DEG, $T = 10$K, $L_z = 40$nm. The solid line corresponds to equation (1.21) and the dashed line corresponds to equation (1.20)

1.3.1 Born approximation

The transmission-reflection states of provide a complete set of states with which we can do perturbation theory. These basis states not orthogonal over the computational

domain – they are orthogonal over the entire x-axis. However, the electric fields due to the top and back gates are localized in space, which makes it possible to exploit the orthogonality of the transmission-reflection states, yet the overlap integrals, necessary to compute the matrix elements, can be carried out inside the finite-sized computational domain.

We now rewrite equation (1.19) in the form

$$\langle J \rangle = \mathrm{Tr}[\hat{J}\hat{\rho}] \tag{1.22}$$

where the density matrix operator is

$$\hat{\rho} = \int dE_x\, dE_y \sum_{n\sigma} f_{n\sigma}(E_x, E_y) \left| E_x E_y n\sigma \right\rangle \left\langle E_x E_y n\sigma \right| \tag{1.23}$$

and the current operator is

$$\hat{J} = \frac{2e}{\hbar} \int dE_x\, dE_y \sum_{n\sigma} \sigma T_{n\sigma}(E_x, E_y) \left| E_x E_y n\sigma \right\rangle \left\langle E_x E_y n\sigma \right| \tag{1.24}$$

Making use of the first-order Born approximation, the basis states in the interaction picture evolve according to

$$\left| k_x k_y n\sigma, t \right\rangle_I = \left| k_x k_y n\sigma, t_0 \right\rangle_I + \frac{1}{i\hbar} \int_{t_0}^{t} dt' \hat{V}_I(t') \left| k_x k_y n\sigma, t' \right\rangle_I , \tag{1.25}$$

where $\hat{V}_I(t)$ is the interaction term due to the oscillating gate potentials in the interaction picture

$$\hat{V}_I(t) = e^{iH_0 t/\hbar} H_1(t) e^{-iH_0 t/\hbar}, \tag{1.26}$$

where H_0 is the Hamiltonian due to the static shape of the conducting channel, and $H_1(t)$ is the Hamiltonian representing the oscillating electric fields, defined below.

We now consider the system in the presence of the time-dependent, external electric fields $\hat{e}_x\mathcal{E}_x(x) + \hat{e}_z\mathcal{E}_z(x)$, varying harmonically in time at frequency $\omega \sim 1$ THz, where both the x- and z-polarized fields are taken to be constant over the y- and z-directions, and $\hat{e}_x$, $\hat{e}_z$ are unit vectors in the x- and z-directions. Small oscillations of top gate voltage causes the magnitudes of $\mathcal{E}_x$ and $\mathcal{E}_z$ vary harmonically in time. This is called the *quasi-static* approximation, which is useful as a crude approximation to the lowest electromagnetic mode of the waveguide that couples the top and back gates to an antenna. We will treat the interaction with the fields of the top and back gates in the electric dipole approximation. 1 THz has a wavelength of about 0.3mm in vacuum, and about 13 times shorter than this in GaAs, which is about 23µm, much larger than the active region, and much larger than the thickness of the quantum well. In the quasi-static limit considered here, the fields at the edges of the active region fall off in just a couple of microns, so the dipole approximation is reasonably justifiable, but less so at 2–3 THz, especially for the source-drain polarized fields at the edges of the active region.

The dipole approximation gives the interaction term

$$\hat{H}_1 = \frac{e}{im\omega}(e^{-i\omega t} - e^{i\omega t})\left\{\mathcal{E}_x(x)\hat{p}_x + \mathcal{E}_z(x)\hat{p}_z\right\}. \tag{1.27}$$

The next steps are substituting the above into equation (1.25), then substituting the result into equation (1.22), and following the usual procedure of introducing a slow turn-on function and taking $t_0 \to -\infty$, then putting in the Pauli exclusion principle by hand.

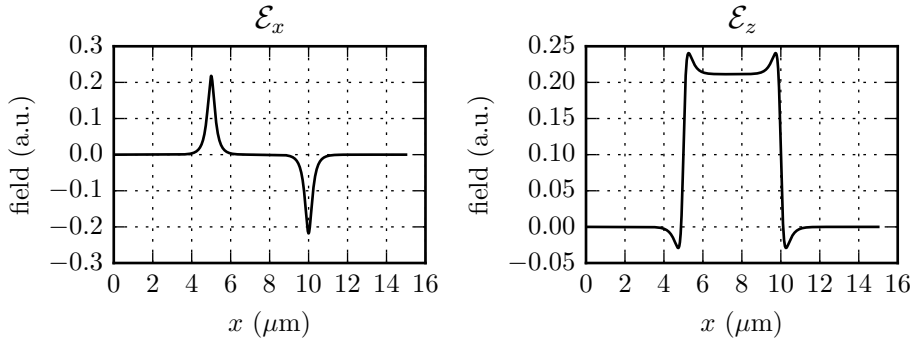

Figure 1.8: The envelopes of the oscillating electric fields due to the top and back gates.

After this is carried out, we arrive at the result $\langle J\rangle = \langle J\rangle_0 + \langle \delta J\rangle$, where

$$\langle \delta J(\omega)\rangle = \frac{2e}{\hbar}\sum_\sigma \sigma \int dE_x\, dE_y \int dE'_x\, dE'_y \sum_{nn'} T_{n'\sigma}(E'_x, E'_y) f_{n\sigma}(E_x, E_y)[1 - f_{n'\sigma}(E'_x, E'_y)] \times 2\pi\delta(E_{xyn\sigma} - E_{x'y'n'\sigma} \pm \hbar\omega) \left|\langle E_x E_y n\sigma|\mathcal{E}_x(x)\hat{p}_x + \mathcal{E}_z(x)\hat{p}_z|E'_x E'_y n'\sigma\rangle\right|^2, \tag{1.28}$$

where $E_{xyn\sigma} = E_x + E_y + E_z^n$ in the reservoir associated with σ. This result is summarized as the Fermi golden rule applied to the Landauer formula.

The shape of the electric fields due to the top and back gates in the quasi-static approximation are shown in Figure 1.8. The matrix elements of the interaction potential (1.27) are shown in Figure 1.9. These off-diagonal matrix elements provide a mechanism by which the TACIT sensor may absorb energy at frequencies below the intersubband resonance, which provides an explanation for some measurements of a recent prototype of the TACIT sensor [4].

The lower-energy states near the bottom-left of the graphs represent states lacking sufficient kinetic energy to enter the active region due to the potential barrier, cf. Figure 1.5. The higher-energy states near the top right of the graphs have entered the active region. The z-element for these states is very sharply peaked when the initial and final

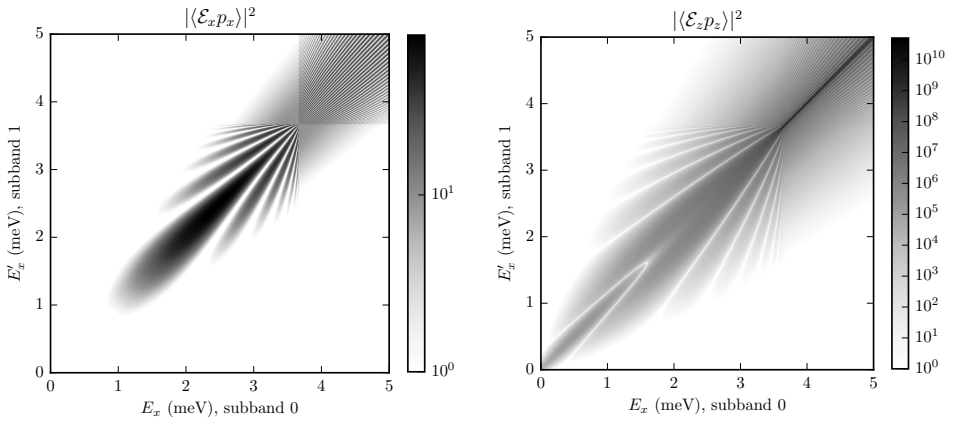

Figure 1.9: The matrix elements for the photoconductivity due to the oscillating top and back gates. (Left) the response due to the x-polarized fields at the edges of the top and back gates. (Right) the response due to the z-polarized fields inside the active region. The horizontal axis shows the value of E_x for the initial electron state in the lowest subband and the vertical axis shows the value of E_x for the final state in the first-excited subbands.

states have the same wavevector. This demonstrates the strength of the *vertical transition*. On the other hand, the x-element does not have a sharp peak for states that enter the active region, instead reveals a fan-like feature for the higher-energy states. These off-diagonal elements are called *indirect transitions*. Another feature of the x-element is that the lower-energy states absorb energy from the electric fields near the edges of the active regions. These features in the x-element can be interpreted as follows: An ingoing electron encounters a twist in the channel along the z-direction due to top and back gates. In the vicinity of the twist, there is also a localized, oscillating source-drain field. The twist in the channel causes the electron to vibrate into the z-direction, a process which is capable of absorbing energy from the localized source-drain field.

There are other quantities that can be calculated perturbatively, such as the photoimpedance, in which the active region is probed in the x-direction by a uniform source-drain field. This suggests a mode of operation for the TACIT detector in the ballistic limit, whereby the energy in the source-drain field can be mixed with the energy in the

field between the top and back gates. However, although it is an interesting effect, this mixing turns out to be very weak. The most interesting aspect of these calculations, from the perspective of this work, is the idea of locally perturbing an infinite system, and computing the response entirely within a finite computational box. If response within the box can be made to agree with the response of the infinite system, this treatment is considered successful. This concept is referred to as *open boundary conditions*. In the interest of pursuing the open boundary conditions more thoroughly, the perturbative model of the TACIT sensor is concluded at this point.

Chapter 2

Perfectly matched layers for the Schrödinger equation

Next, we address the simulation of the time evolution of open quantum systems. We will use this chapter to give some background and review the existing results in the wave-function approach before moving on the density matrix in the next chapter. Restricting our attention to a single subband of the subband-mixing Schrödinger equation derived in Chapter 1, the quantum state $\psi(x)$ evolves according to the usual one-dimensional Schrödinger equation. Our goal is to simulate the Schrödinger equation on a finite computational domain, but for the numerical solution to match the solution computed on an infinite domain. This is difficult to accomplish accurately with ad-hoc methods, such as the introduction of a complex potential term. Since the solutions of the Schrödinger equation are highly oscillatory, and it is difficult to damp out the oscillations without inducing reflections. Two methods currently exist which address the issue: The discrete transparent boundary condition (DTBC) of Arnold et al. [2], and the method of perfectly matched layers (PMLs) of Duru and Kreiss [5]. In this chapter, we will review the method of perfectly matched layers.

2.1 Motivation

Consider the free Schrödinger equation in the units of Appendix C.1

$$i\partial_t \psi(x,t) = -\tfrac{1}{2}\partial_x^2 \psi(x,t). \tag{2.1}$$

The rightward-propagating plane wave $\psi(x,t) = e^{-i(k_0 x - \omega_0 t)}$ is a solution of the above if $\frac{1}{2}k_0^2 = \omega_0$, where k_0 and ω_0 are both positive real numbers. We now consider the Fourier transform in time of the plane wave solution

$$\hat{\psi}(x,\omega) = \int dt\, e^{-i\omega t}\psi(x,t). \tag{2.2}$$

The Fourier-transformed plane wave is written in the form

$$\hat{\psi}(x,\omega) = 2\pi\delta(\omega-\omega_0)e^{-i\omega\kappa x}, \tag{2.3}$$

where $\kappa = k/\omega$. We now attempt to modify the Schrödinger equation such that the plane wave solution is decaying on the half space $x > 0$. This will occur if the solution is modified to

$$\hat{\psi}(x,\omega) \to 2\pi\delta(\omega-\omega_0)e^{-\kappa\Gamma(x)}e^{-i\omega\kappa x}, \tag{2.4}$$

where $\Gamma(x)$ is a monotonically increasing, smooth, real function of x with $\Gamma = 0$ if $x \leq 0$, and $\Gamma > 0$ for $x > 0$. Rewriting equation (2.4) as

$$\hat{\psi}(x,\omega) \to 2\pi\delta(\omega-\omega_0)e^{-i\omega\kappa\left(x+\frac{\Gamma(x)}{i\omega}\right)} \tag{2.5}$$

we observe that the mapping

$$x \to x + \tfrac{\Gamma(x)}{i\omega} \tag{2.6}$$

gives a decaying wave for $x > 0$, while the solution for $x \leq 0$ is unchanged.

2.2 Coordinate stretching formulation

With this motivation, consider the Fourier-transformed free Schrödinger equation

$$i(i\omega)\hat{\psi}(x,\omega) = -\tfrac{1}{2}\partial_x^2\hat{\psi}(x,\omega). \tag{2.7}$$

Under the change of coordinates $x \to x + \Gamma(x)/i\omega$, the partial derivative with respect to x changes to $\partial_x \to s^{-1}\partial_x$, where $s = 1 + \sigma(x)/i\omega$ and $\sigma(x) = d\Gamma(x)/dx$. Applying this change of variables to equation (2.7), we have

$$i(i\omega)\hat{\psi}(x,\omega) = -\frac{1}{2}\frac{1}{s}\frac{\partial}{\partial x}\frac{1}{s}\frac{\partial}{\partial x}\hat{\psi}(x,\omega). \tag{2.8}$$

We now transform equation (2.8) back into the time domain. Multiplying both sides by s, we have

$$i(i\omega)\left(1 + \frac{\sigma}{i\omega}\right)\hat{\psi}(x,\omega) = -\tfrac{1}{2}\partial_x^2\hat{\psi}(x,\omega) + \tfrac{1}{2}\partial_x(\sigma\hat{u}(x,\omega))$$

where u, an *auxiliary variable*, has been defined as

$$\hat{u}(x,\omega) = \frac{1}{s}\frac{\partial_x\hat{\psi}(x,\omega)}{i\omega}$$

We transform back to the time domain by eliminating all the factors of $i\omega$ appearing in the denominator and then making the replacement $i\omega\hat{f}(x,\omega) \to \partial_t f(x,t)$, where $f \in \{\psi, u\}$.

Assuming that the potential term is constant near over the absorbing layers and outside the computational domain, it does not affect the PML. Adding the potential term, the Schrödinger equation with PMLs is

$$\begin{cases} i\partial_t \psi(x,t) = (-\frac{1}{2}\partial_x^2 + v(x))\psi(x,t) + \frac{1}{2}\partial_x(\sigma u(x,t)) - i\sigma\psi(x,t) \\ \partial_t u(x,t) \;\; = -\sigma u(x,t) + \partial_x \psi(x,t) \end{cases} \tag{2.9}$$

So far, we have been treating the problem of absorbing the outgoing waves in the half space $x > 0$. However, at this point we can pad the computational box with two short intervals, called the *absorbing layers*, set $\sigma = 0$ over the active region and have σ smoothly increase from zero as it approaches the edges of the computational box. Then outgoing waves will be absorbed at either end of the computational box with controllable errors.

2.3 Discretization

Equations (2.9) are discretized in time according to the Crank-Nicolson scheme, and according to the second-order centered difference scheme in space, with homogeneous Dirichlet boundary conditions at the endpoints. For a brief outline of the Crank-Nicolson method, see Appendix C.3. This yields a numerical scheme which is unitary over the interior of the computational domain, unconditionally stable, and locally of second order accuracy in time and space. Duru and Kreiss developed a spatially fourth-order accurate scheme, and hence their error terms are somewhat smaller [5].

We begin by discretizing in time. Consider a single time step of size h_t. Let $\{\psi^n(x),\ u^n(x)\}$ and $\{\psi^{n+1}(x),\ u^{n+1}(x)\}$ be the initial and final wavefunctions and aux-

iliary fields repectively. On the lefthand side of equation (2.9), we make the replacement

$$\begin{cases} \partial_t \psi(x,t) \rightarrow \dfrac{\psi^{n+1}(x) - \psi^n(x)}{h_t} \\ \partial_t u(x,t) \rightarrow \dfrac{u^{n+1}(x) - u^n(x)}{h_t}. \end{cases} \tag{2.10}$$

On the righthand side of equation (2.9), we make the replacement

$$\begin{cases} \psi(x,t) \rightarrow \dfrac{\psi^n(x) + \psi^{n+1}(x)}{2} \\ u(x,t) \rightarrow \dfrac{u^n(x) + u^{n+1}(x)}{2} \end{cases} \tag{2.11}$$

Next, the auxiliary field u^{n+1} is isolated in the second line of equation (2.9)

$$u^{n+1}(x) = \frac{-\frac{1}{2}h_t\sigma(x)u^n(x) + \frac{1}{2}h_t\partial_x\psi^n(x) + \frac{1}{2}h_t\partial_x\psi^{n+1}(x) + u^n(x)}{1 + \frac{1}{2}h_t\sigma(x)/2}. \tag{2.12}$$

The result is substituted into the first line of equation (2.9). This gives a rather long expression involving $\{\psi^{n+1}(x),\ \psi^n(x),\ u^n(x)\}$, as well as their first and second spatial derivatives. It is desirable to use a computer algebra system to perform these substitutions, and then generate the numerical routines automatically from the symbolic expressions. The x-dependence of the fields is discretized onto a uniform grid $\{x_j\},\ j = 1...N_x$ with spacing h_x, so that $x_j = jh_x$. The spatial derivatives are approximated using the second-order centered difference scheme,

$$\begin{aligned} \frac{\partial f}{\partial x}(x_j) &\rightarrow \frac{f(x_{j+1}) - f(x_{j-1})}{2h_x}, \\ \frac{\partial^2 f}{\partial x^2}(x_j) &\rightarrow \frac{f(x_{j+1}) + f(x_{j-1}) - 2f(x_j)}{h_x^2}, \end{aligned}$$

for any smooth function $f(x)$. This yields a matrix equation for $\psi^{n+1}(x_j)$

$$\sum_{j'} T_{j,j'} \psi^{n+1}(x_{j'}) = r(x_j; \psi^n(x_j), u^n(x_j))$$

where $T_{j,j'}$ is a tridiagonal matrix and $r(x_j; \psi^n(x_j), u^n(x_j))$ represents the righthand side given by the procedure outlined above. Then ψ^{n+1} may be found using Gaussian elimination in $O(N_x)$ steps. The result is substituted into the discrete form of the second line of equation (2.9), which is solved for u^{n+1}.

We note that the same basic method can be applied to the 2d Schrödinger equation with similar accuracy and stability results. For efficiency, an alternating-direction implicit method should be used to invert the matrix on the lefthand side in the two-dimensional case [6].

2.4 Simulation results

We demonstrate the accuracy of the PML using two numerical tests. First, we compare the numerical evolution of equation (2.9) against the analytic evolution of a Gaussian wave packet for $v(x) = 0$, which is derived in Appendix C.2.

$$\psi(x,t) = \frac{\mathcal{N}}{\sqrt{2\pi}} \frac{1}{\sqrt{\sigma^2 - it}} \exp\left[-\frac{\frac{1}{2}x^2 + i\sigma^2(k_0 x - \frac{1}{2}k_0^2 t)}{\sigma^2 - it} \right]$$

The time step is adjusted until the local errors due to the finite difference scheme are made significantly smaller than the errors due to reflections from the PML. The spatial grid is refined with the number points in the absorbing layer N_b equal to one eigth of the total number of points. The strength of the reflections is observed to decreases roughly as $O(N_x^{-2})$ for small initial wavevectors k_0 and sub-second-order accuracy for the larger initial wavevectors.

Relative error, numerical vs exact ($v = 0$)

k_0 (nm^{-1})	$N_x = 256$ $N_b = 32$	$N_x = 512$ $N_b = 64$	$N_x = 1024$ $N_b = 128$
0.	4.20×10^{-3}	1.36×10^{-3}	6.40×10^{-4}
0.296	4.30×10^{-3}	8.94×10^{-4}	3.69×10^{-4}
1.479	8.73×10^{-3}	3.23×10^{-4}	3.07×10^{-4}

Table 2.1: Relative error between the numerical solution of the Schrödinger equation with PMLs with the exact solution for Gaussian wavepackets initialized with $\sigma = 1.69$ nm and various values of k_0, with x_0 near the center of the domain of length $L_x = 33.8$ nm. Each solution is propagated in time for 19.8 fs with a time step of $h_t = 6.58 \times 10^{-3}$ fs.

Relative error, numerical vs reference ($v_b = 1000$ meV)

k_0 (nm^{-1})	$N_x = 256$ $N_b = 32$	$N_x = 512$ $N_b = 64$	$N_x = 1024$ $N_b = 128$	$N_x = 2048$ $N_b = 256$
0.296	4.570×10^{-3}	1.23×10^{-3}	3.15×10^{-4}	7.91×10^{-5}

Table 2.2: Relative error between the numerical solution of the Schrödinger equation with PMLs and the standard Crank-Nicolson discretization over a much larger domain. The potential barrier is of height $v_b = 1000$ meV and 3 nm in width. Unless otherwise indicated, the rest of the parameters are the same as in Table 2.4

The presence of a potential bump does not affect the accuracy of the PML, provided the potential is constant within the absorbing layers. In order to check the accuracy including the potential bump, we solve equation (2.9) over a smaller domain and compare the solution against the second-order Crank-Nicolson solution of the Schrödinger equation without PMLs simulated over a much larger domain (see Appendix C.3). We can see again that the strength of the reflections decreases roughly as $O(N_x^{-2})$.

2.5 Discussion and future directions

We have confirmed that PMLs for the Schrödinger equation are capable of accurately simulating the time evolution of wave packets initialized inside the active region with open boundary conditions. However, in order to simulate a microstructure coupled to a thermal reservoir, we must account for the presence of an incoming state ψ_{res}, which is the solution of Schrödinger's equation inside the reservoir. Taking the potential inside the reservoir to be zero, the Hamiltonian inside the reservoir is $H_{\text{res}} = -\frac{1}{2}\partial_x^2$, and the solution of Schrödinger's equation inside the reservoir is

$$\psi_{\text{res}}(x,t) \sim e^{-i(k_0 x - \frac{1}{2}k_0^2 t)}, \tag{2.13}$$

where k_0 is the wave vector. We will assume that the active region does not support any bound states, but it may contain a potential bump $v(x,t)$, whose shape could vary in time, where $v(x,t) = 0$ inside the reservoirs. Then the total Hamiltonian inside the active region is $H_{res} + v(x,t)$

An important direction for future research is computing the response of the reservoir wavefunction to the potential bump localized within the active region. If $v(x,t)$ did not depend on time, then in the limit of long times the total wavefunction will approach a solution of the transmission-reflection problem. Writing the total wavefunction as $\psi_{\text{res}} + \psi_{\text{act}}$, where ψ_{act} is associated with the perturbation inside to the active region, we see that its time evolution is given by

$$i\partial_t(\psi_{\text{res}} + \psi_{\text{act}}) = (H_{\text{res}} + v(x,t))(\psi_{\text{res}} + \psi_{\text{act}}). \tag{2.14}$$

Since $i\partial_t \psi_{\text{res}} = H_{\text{res}} \psi_{\text{res}}$, the above may be simplified to

$$i\partial_t \psi_{\text{act}} = (H_{\text{res}} + v(x,t))\psi_{\text{act}} + v(x,t)\psi_{\text{res}}. \tag{2.15}$$

We see that the fluctuations away from the reservoir wavefunction are given by the usual Schrödinger equation inside the active region plus a source term localized to the active region. Hence the total wavefunction may be computed by solving equation (2.15) with PMLs. It would be interesting to see whether a transmission-reflection state could be recovered from the time-evolution of equation (2.15).

Chapter 3

Perfectly matched layers for the Liouville von Neumann equation

In order to simulate a device in which the active region is immersed in a bath of transmission-reflection states, it is necessary to account for a very large number of these states, effectively a continuum of them, which together resolve the local electron density. This approach has been successfully applied to nanoscale structures such as resonant tunneling diodes in the ballistic limit [7, 8]. However, the number N_e of transmission-reflection states necessary is arbitrarily large. Evolving each of these states in time using the methods of the previous chapter would result in a total computational complexity scaling as $O(N_e N_x)$.

It is highly desirable to evolve the density matrix in time, instead of the wavefunctions. Once the active region is discretized into some number of points N_x making up the computational domain, the methods derived here demonstrate that the density matrix may be evolved in time at a fixed computational complexity of $O(N_x^2 \log N_x)$. Furthermore, compared with wavefunction methods, the density matrix approach described here is much more amenable to the inclusion of scattering terms, which are necessary for

a more realistic model of a semiconductor heterostructure that may depart from the ballistic limit.

In this chapter, perfectly matched layers (PMLs) will be developed for the position-space density matrix. The approach given here appears to be an original solution to the problem of simulating the distribution function of a microscopic device using a so-called phase-space approach. It took some trial and error to arrive at this approach, and it is interesting to put the results of this chapter into some context.

The first attempt was to follow the approach of Arnold, Ringhofer, and Frensley, et al. [9, 10, 11], and compute the time-evolution of the discrete Wigner function. The Wigner function $w(x, k, t)$ is related to the position-space density matrix $\rho(x_1, x_2, t)$ by rotating and scaling the coordinate system, followed by a spatial fourier transform

$$w(x, k, t) = \int d\eta \; e^{ik\eta} \rho(x + \tfrac{1}{2}\eta, x - \tfrac{1}{2}\eta, t) \tag{3.1}$$

It evolves in time according to

$$\frac{\partial w(x,k)}{\partial t} + \frac{\hbar k}{m}\frac{\partial w(x,k)}{\partial x} + \frac{1}{\hbar}\int \frac{dk}{2\pi} \mathcal{V}(x, k - k') w(x, k') = 0, \tag{3.2}$$

where

$$\mathcal{V}(x, q) = 2 \int d\eta \; \sin(q\eta)[v(x + \tfrac{1}{2}\eta) - v(x - \tfrac{1}{2}\eta)] \tag{3.3}$$

and v is the potential energy. It was observed over the course of this work that the discretized Wigner evolution equation was unable to recover the stationary solution of the transmission-reflection problem, and hence unable to accurately capture the ballistic limit. The essential reason for this is the Wigner function suffers from a property called *filamentation*: Consider the case of $v = 0$ and the unit system of Appendix C.1. Then

equation (3.2) reduces to

$$\partial_t w + k\partial_x w = 0. \tag{3.4}$$

Suppose that the initial condition takes the form of a spatially-modulated Maxwellian distribution

$$w(x,k,0) = w_0(x,k) = [1 + A\cos(k_0 x)]e^{-k^2/2}. \tag{3.5}$$

Then the solution at time t is

$$w(x,k,t) = w_0(x-kt,k) = [1 + A\cos(k_0 x - k_0 kt)]e^{-k^2/2}. \tag{3.6}$$

The "wavelength" of this function along k-direction is $\lambda_k = 2\pi/k_0 t$. After sufficient time has passed, λ_k must grow smaller than the resolution of the (x,k) numerical grid. This leads to aliasing effects and uncontrolled errors.

Eliasson simulated the classical limit $\hbar \to 0$ of the Wigner evolution equation, which is equivalent to the Boltzmann equation [12, 42]. He observed that the Fourier transform of the Wigner function

$$f(x,\eta) = \rho(x + \tfrac{1}{2}\eta, x - \tfrac{1}{2}\eta) \tag{3.7}$$

does not suffer from filamentation but instead grows smoother with increasing time under free evolution. He worked with periodic boundary conditions in the x-direction and developed a projection technique to absorb outgoing fluctuations at the edge of the η-direction. In order to implement open boundary conditions in this work, it was attempted to use Eliasson's projection method at the edges of the computational domain in the x-

direction. However, the projection method resulted in uncontrolled ringing artifacts. The perfectly-matched layer approach described below is able to effectively control the strength of the reflections at the edges of the computational domain.

Another question to consider is the following: *Why the position-space density matrix, instead of the energy-space density matrix?* Let's attempt to flesh out the energy-space time-evolution further: Suppose one had computed a complete basis of transmission-reflection for a self-consistent treatment of a micro-structure. The dynamical variables would be the correlations between the various wavevectors of ingoing states associated with the left- and right reservoirs. There are two major technical challenges with this approach:

- The basis of energy eigenstates requires arbitrarily fine energy resolution in order to accurately represent the time evolution of the density matrix.
- The overlap integrals necessary to compute the scattering rates require integration over infinite intervals. It may be possible to compute them accurately. Some effort was made to compute these integrals could within Fourier space, but the results were rather cumbersome.

For example, consider a sequential-tunneling superlattice, as described in Chapter 4. Each peak of the transmission function $T(E)$ is by definition very narrow, and the energy coordinate of the peak evolves in time, implying that it is necessary to use either an arbitrarily large number of basis states would be necessary, or a non-unifom energy grid would be necessary to evolve as a function of time. This generalizes the ideas of MacLennan and Abdallah to the time-dependent problem [7, 8].

On the other hand, the position-space density matrix remains smooth, its transients growing smoother in time. The amount of data necessary to numerically represent it is controlled: It depends only on the energy scale of the quantum transitions involved in

the time evolution, and the length of the computational domain. Scattering terms are included naturally at the semiclassical level with the Wigner function and the Fermi golden rule. The position-space density matrix approach is extremely simple in comparison to the energy-space approach outlined above.

3.1 Evolution equation

Consider the time evolution of the one-body density matrix in one dimension with a time-independent potential term. In the units of Appendix C.1, the usual Liouville-von Neumann equation for the time evolution of the density matrix is

$$i\partial_t \rho(x_1, x_2, t) = \left[-\tfrac{1}{2}(\partial_1^2 - \partial_2^2) + v(x_1) - v(x_2)\right] \rho(x_1, x_2, t),$$

where ∂_1 and ∂_2 correspond to differentiation with respect to the first and second arguments of $\rho(\cdot, \cdot, t)$ respectively. Interestingly, numerical experiments have shown that the PML procedure outlined for the Schrödinger equation in Chapter 2 fails for the density matrix in the x_1-x_2 coordinates. The reason appears to be that the wavefronts impinge on the boundary layer at too shallow of an angle. However, it will be shown that in a transformed coordinate system, the PML is well-behaved. The transformation is written as

$$\begin{cases} x_1 \to x + \frac{1}{2}\eta \\ x_2 \to x - \frac{1}{2}\eta. \end{cases} \tag{3.8}$$

A visual representation this transformation is shown in Figure 3.1. In the new coordi-

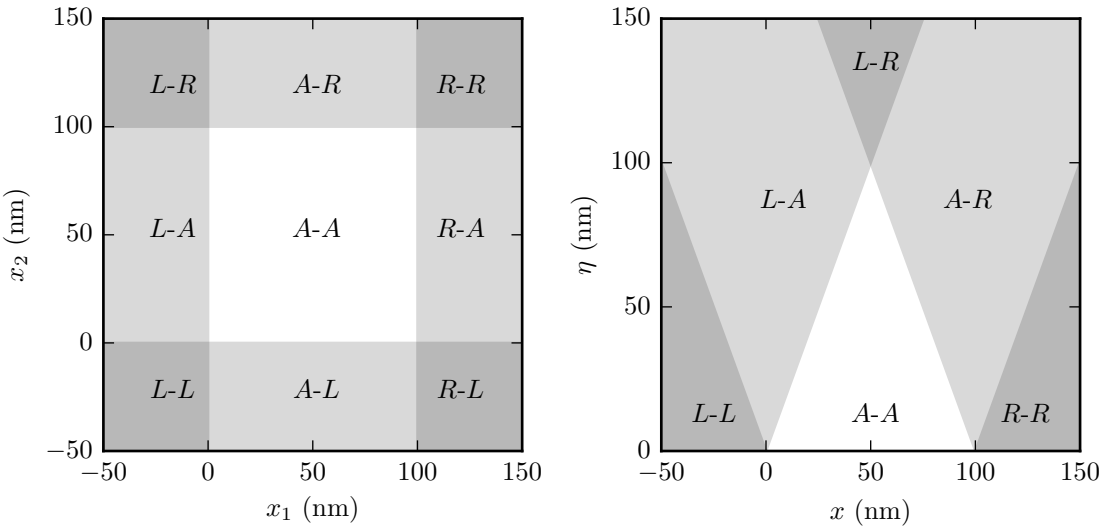

Figure 3.1: The coordinate transformation of equation (3.8) on a 100 nm computational domain. The shaded regions correspond to spatial correlations between the active region (A), left contact (L) and right contact (R), have been labeled accordingly

nates, the Liouville-von Neumann equation is

$$i\partial_t \rho(x+\tfrac{1}{2}\eta, x-\tfrac{1}{2}\eta, t) = \left[-\tfrac{1}{2}(\partial_1^2 - \partial_2^2) + v(x+\tfrac{1}{2}\eta) - v(x-\tfrac{1}{2}\eta)\right] \rho(x+\tfrac{1}{2}\eta, x-\tfrac{1}{2}\eta, t).$$

Making use of the identities

$$\partial_x \rho(x+\tfrac{1}{2}\eta, x-\tfrac{1}{2}\eta, t) = (\partial_1 + \partial_2)\rho(x+\tfrac{1}{2}\eta, x-\tfrac{1}{2}\eta, t)$$

$$\partial_\eta \rho(x+\tfrac{1}{2}\eta, x-\tfrac{1}{2}\eta, t) = \tfrac{1}{2}(\partial_1 - \partial_2)\rho(x+\tfrac{1}{2}\eta, x-\tfrac{1}{2}\eta, t)$$

the Liouville-von Neumann equation in the transformed coordinates is

$$i\partial_t \rho(x+\tfrac{1}{2}\eta, x-\tfrac{1}{2}\eta, t) = \left[-\partial_x\partial_\eta + v(x+\tfrac{1}{2}\eta) - v(x-\tfrac{1}{2}\eta)\right] \rho(x+\tfrac{1}{2}\eta, x-\tfrac{1}{2}\eta, t) \quad (3.9)$$

and Equation (3.9) is rewritten as

$$\partial_t f(x,\eta,t) = i\partial_x\partial_\eta f(x,\eta,t) - i\delta v(x,\eta) f(x,\eta,t), \tag{3.10}$$

where

$$f(x,\eta,t) = \rho(x+\tfrac{1}{2}\eta, x-\tfrac{1}{2}\eta, t) \tag{3.11}$$

and

$$\delta v(x,\eta) = v(x+\tfrac{1}{2}\eta) - v(x-\tfrac{1}{2}\eta). \tag{3.12}$$

3.2 Perfectly matched layers

We now implement PMLs for equation (3.10), following the same procedure as with the Schrödinger equation. However, there is one inconvenient point: The potential term in the LvN equation is not of a compact shape; it extends off to infinity. Hence it is not possible to surround the computational domain with a layer in which the potential term is constant. In practice, it is desirable to cut off the large-η correlations of the density matrix before they reach the top boundary shown on the right of Figure 3.1. However, in this work we will make a quantitative comparison with the ballistic limit, in order to characterize the largest possible sources of error.

We begin by neglecting the potential term and Fourier transforming equation (3.10) in time

$$i\omega\hat{f}(x,\eta,\omega) = i\partial_x\partial_\eta\hat{f}(x,\eta,\omega) \tag{3.13}$$

Next we introduce the change of coordinates

$$\begin{cases} x \to x + \dfrac{\Gamma_x(x)}{i\omega}, \\ \eta \to \eta + \dfrac{\Gamma_\eta(\eta)}{i\omega}. \end{cases} \tag{3.14}$$

Then equation (3.10) becomes

$$i\omega \hat{f}(x,\eta,\omega) = i s_x^{-1} \partial_x s_\eta^{-1} \partial_\eta \hat{f}(x,\eta,\omega), \tag{3.15}$$

where $s_x = 1 + \sigma_x(x)/i\omega$, $s_\eta = 1 + \sigma_\eta(\eta)/i\omega$, and $\sigma_x(x) = d\Gamma_x(x)/dx$, $\sigma_\eta = d\Gamma_\eta(\eta)/d\eta$. The σ functions are both zero over the interior of the computational domain and increase over the absorbing layers. Since s_η commutes with ∂_x, equation 3.15 is equivalent to

$$\left(i\omega + \sigma_x + \sigma_\eta + \frac{\sigma_x \sigma_\eta}{i\omega} \right) \hat{f}(x,\eta,\omega) = i \partial_x \partial_\eta \hat{f}(x,\eta,\omega) \tag{3.16}$$

Introducing the auxiliary field ϕ, where

$$\hat{\phi}(x,\eta,\omega) = \frac{\hat{f}(x,\eta,\omega)}{i\omega}, \tag{3.17}$$

the evolution equation is mapped back into the time domain and the potential term is re-inserted, which gives the Liouville-von Neumann equation with PMLs

$$\begin{cases} \partial_t f(x,\eta,t) = [i\partial_x \partial_\eta - i\delta v - (\sigma_x + \sigma_\eta)] f(x,\eta,t) - \sigma_x \sigma_\eta \phi(x,\eta,t) \\ \partial_t \phi(x,\eta,t) = f(x,\eta,t). \end{cases} \tag{3.18}$$

3.3 Operator splitting method

The Liouville-von Neumann equation is propagated in time using the method of operator splitting [9]. If the kinetic term in equation (3.18) is neglected, this gives

$$\begin{cases} \partial_t f(x,\eta,t) = [-i\delta v - (\sigma_x + \sigma_\eta)] f(x,\eta,t) - \sigma_x \sigma_\eta \phi(x,\eta,t) \\ \partial_t \phi(x,\eta,t) = f(x,\eta,t), \end{cases} \tag{3.19}$$

which is straightforward to discretize over the position space coordinates (x, η). If everything except for the kinetic term in equation (3.18) is neglected, this gives

$$\begin{cases} \partial_t f(x,\eta,t) = i\partial_x \partial_\eta f(x,\eta,t) \\ \partial_t \phi(x,\eta,t) = 0. \end{cases} \tag{3.20}$$

Since equation (3.20) comprises a 2d hyperbolic PDE, a high-resolution numerical method is necessary in order to propagate it accurately in time. A spectral method, outlined below, is used for this purpose:

Defining a map from position space to momentum space

$$\tilde{f}(q,k,t) = \int dx d\eta \; e^{i(qx+k\eta)} f(x,\eta,t), \tag{3.21}$$

equation (3.20) takes the form

$$\begin{cases} \partial_t \tilde{f}(q,k,t) = iqk\tilde{f}(q,k,t) \\ \partial_t \phi(x,\eta,t) = 0, \end{cases} \tag{3.22}$$

which is straightforward to discretize over momentum space coordinates (q, k). Assuming that $f(x, \eta)$ remains a sufficiently smooth function for all time, $\tilde{f}(q, k)$ will rapidly decay

to zero for high values of $|q|$ and $|k|$. Additionally, due to the presence of the PML, $f(x, \eta)$ will smoothly decay to zero before it reaches the edges of the computational domain. These two conditions allow for the imposition of periodic boundary conditions on the computational domain, while the numerical solution evolves under open boundary conditions. The mapping from f to $\tilde{f}$ is accomplished efficiently using the fast Fourier transform.

Let h_t be the size of the time step, so that the discrete time variable is $t_s = sh_t$. The discrete time evolution will consist of two steps:

1. A "kinetic step," during which f solves equation (3.22) with the initial condition $f = f(x, \eta, t_s)$. The solution after time h_t is called $f(x, \eta, t_{s+1/2})$.

2. A "potential step," during which $\hat{f}$ solves equation (3.19) with the initial condition $f = f(x, \eta, t_{s+1/2})$. The solution after time h_t is called $f(x, \eta, t_{s+1})$.

Setting $f(x, \eta, t_{s+1}) = f(x, \eta, t_s + h_t)$ results in a scheme that is locally first-order accurate in time. For a second order scheme, we start by calculating $f(x, \eta, t_{s+1})$ as given above. Then, exchanging the order of the kinetic and potential steps, we calculate $\hat{f}(x, \eta, t_{s+1})$ again, and take the arithmetic mean of the two results. The first- and second-order splitting schemes are identical to one another in the case of zero potential. While the second order method does improve the local accuracy of the splitting scheme, the spectral accuracy of the first-order method is already much better than the finite-difference Crank-Nicolson method used for the reference solution in the simulation results below. The largest errors of this numerical method are due to the suboptimal performance of the PML for nonzero potential functions, but even these errors remain within 1% or so of the reference solution in the test cases below.

In order to have unitary evolution on the interior of the computational domain, the temporal discretization makes use of the Crank-Nicolson method for each part of the

split time step. For the potential step, this results in the set of equations

$$\begin{cases} f^{s+1}(x,\eta) = -h_t\phi^s(x,\eta)\sigma_x(x)\sigma_y(\eta) \\ \qquad\qquad + \left(\dfrac{-\frac{1}{4}h_t^2\sigma_x\sigma_y - \frac{i}{2}h_t\delta v(x,\eta) - \frac{1}{2}h_t(\sigma_x+\sigma_y)+1}{\frac{1}{4}h_t^2\sigma_x\sigma_y + \frac{i}{2}h_t\delta v(x,\eta) + \frac{1}{2}h_t(\sigma_x+\sigma_y)+1}\right) f^s(x,\eta) \\ \phi^{s+1}(x,\eta) = \frac{1}{2}h_t f^s(x,\eta) + \frac{1}{2}h_t f^{s+1}(x,\eta) + \phi^s(x,\eta) \end{cases} \tag{3.23}$$

For the kinetic step, this results in the set of equations

$$\begin{cases} \tilde{f}^{s+1}(q,k) = \dfrac{-\frac{i}{2}h_t qk + 1}{\frac{i}{2}h_t qk + 1}\hat{f}^s(q,k) \\ \phi^{s+1}(x,\eta) = \phi^s(x,\eta). \end{cases} \tag{3.24}$$

3.4 Simulation results

3.4.1 Free evolution

The first test considered is the free evolution of a Gaussian wave packet with $v = 0$. In this case the error is calculated by comparing the numerical density matrix against the density matrix formed from the exact solution of the Schrödinger equation.

$$\psi(x,t) = \frac{\mathcal{N}}{\sqrt{2\pi}}\frac{1}{\sqrt{\sigma^2 - it}}\exp\left[-\frac{\frac{1}{2}x^2 + i\sigma^2(k_0 x - \frac{1}{2}k_0^2 t)}{\sigma^2 - it}\right], \tag{3.25}$$

where $\mathcal{N}$ is a normalization factor. For comparison, the density matrix $f(x,\eta,t)$ is formed from $\psi(x,t)$ according to

$$f(x,\eta,t) = \psi(x+\tfrac{1}{2}\eta,t)\psi^*(x-\tfrac{1}{2}\eta,t). \tag{3.26}$$

The density matrix is initialized with a gaussian wave packet, propagated in time numerically, and compared against the exact density matrix computed from the equation

Relative error, numerical vs exact ($v = 0$)

k_0 (nm^{-1})	$N_b = 8$	$N_b = 16$	$N_b = 32$	$N_b = 64$
0.	2.49×10^{-3}	1.58×10^{-4}	3.35×10^{-6}	1.07×10^{-6}
0.296	3.63×10^{-3}	2.55×10^{-4}	3.80×10^{-6}	1.13×10^{-6}
1.479	6.19×10^{-1}	6.13×10^{-3}	4.57×10^{-5}	8.54×10^{-6}

Table 3.1: Comparing the numerical solution of the LvN equation with PMLs with the exact solution for Gaussian wavepackets initialized with $\sigma = 1.69$ nm and various values of k_0, with x_0 near the center of the domain of length $L_x = 33.8$ nm. Each solution is propagated in time for 39.5 fs with a time step of $h_t = 6.58 \times 10^{-3}$ fs. The dimensions of the computational grid are $N_x = N_y = 512$, and N_b is the number of points in the absorbing layer.

above. The results of the simulations are listed in Table 3.4.1. The higher the energy of the state, the lower the accuracy of the PML. However, the accuracy of the PML improves rapidly as the layer is widened. In fact, the accuracy of the PML for the Liouville-von Neumann equation scales much more favorably than the numerical experiments for the Schrödinger equation in Chapter 2. This is due to the use of a second-order scheme for the Schrödinger equation compared with a spectral scheme for the LvN equation.

Similar numerical experiments also demonstrated that two separate initial conditions of Schrödinger's equation can be combined into a single initial condition for the the Liouville-von Neumann equation and evolved in time with similar accuracy. This demonstrates one advantage of the density matrix approach: With sufficient floating-point accuracy, an arbitrarily large number of pure states could be combined into a single mixed state, which can be evolved in time at a *fixed* computational cost.

3.4.2 Interaction with a potential barrier

The behavior of the PML in the presence of a nonzero potential term is tested next. The LvN equation is again initialized with a Gaussian wave packet. Then the solution of the LvN equation is compared against the density matrix formed from the solution of

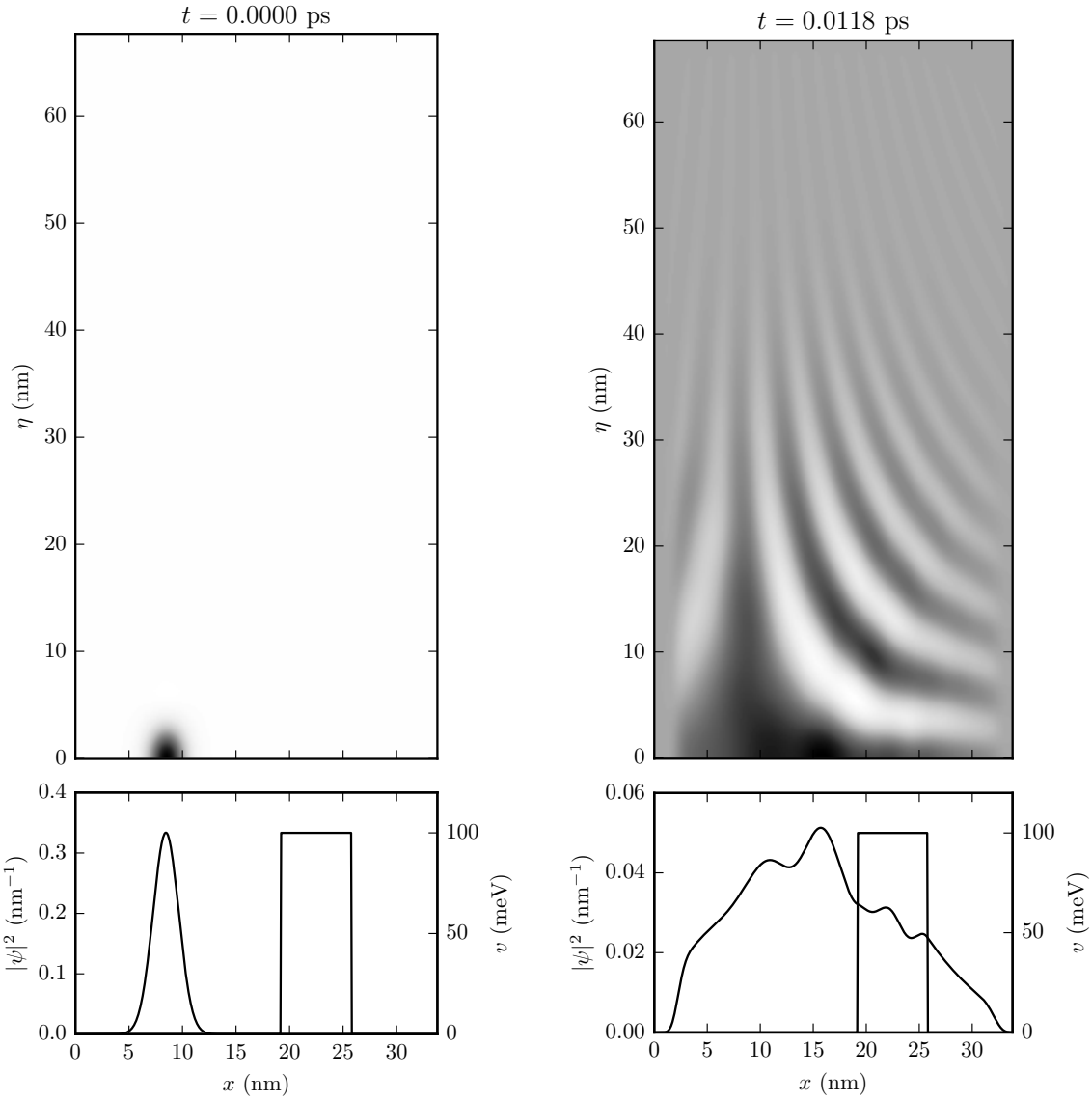

Figure 3.2: Snapshots of the initial state and an intermediate state of the time-evolution of the Liouville-von Neumann equation initialized with a Gaussian wavepacket with $k_0 = 1.479$ nm^{-1} and $N_b = 64$, as listed in Table 3.4.1. The top frames show the amplitude of the real part of the density matrix, where darker colors correspond to more positive values. In the right column, the zero of the color map corresponds to a medium grey. The bottom frames plot the diagonal elements of the density matrix as well as the square potential barrier. The solution can be observed to decay to zero inside the absorbing layers on the righthand column.

Relative error, LvN vs Schrödinger

v_b (meV)	$N_b = 8$	$N_b = 16$	$N_b = 32$	$N_b = 64$
0	4.84×10^{-3}	3.70×10^{-4}	3.65×10^{-5}	2.59×10^{-5}
10	6.33×10^{-3}	5.49×10^{-3}	5.02×10^{-3}	5.54×10^{-3}
100	6.65×10^{-2}	6.02×10^{-2}	5.83×10^{-2}	5.34×10^{-2}

Table 3.2: Propagation error in the presence of a square potential barrier of length 6.6 nm and height v_b, located near the right side of the domain. Comparing the numerical solution of the LvN equation with PMLs against the density matrix formed from the higher-resolution Crank-Nicolson propagation of Schrödinger's equation on a much larger domain. The simulation parameters are the same as in Table 3.4.1 with $k_0 = 0.296$ nm^{-1}, except x_0 is near the left side of the domain instead of the center, and the dimensions of the computational grid are $N_x = 512$, $N_y = 1024$.

Schrödinger's equation initialized with the same gaussian wave packet on a much larger domain, with four times the resolution in space and ten times the resolution in time. Comparing the first row of Table 3.4.2 against the second row of Table 3.4.1, we can see that the "baseline" error of the Crank-Nicolson method for Schrödinger's equation is somewhat larger than the accuracy of the spectral scheme for the LvN equation in the case of $v = 0$.

The main source of error is due to the interaction of the potential term with the PML. This error dominates over the local errors due to the splitting scheme. We noticed that if the potential term overlaps with the absorbing layer at the top of the computational domain, the errors are greater than those associated with the left and right edges. The reason is that the numerical reflections along the top edge are more able to pollute the interior of the domain. In contrast, numerical reflections at the left and right edges of the domain tend to stay more confined to the edges. For this reason, the intersections of the potential term with the top of the domain were avoided by doubling the length of the computational box in the η direction, cf. Figure 3.1

The PML performs within a few percent accuracy in the presence of the potential

barrier of up to 100 meV. The error reported in Table 3.4.2 turns out to be the relative error at the end of the time evolution interval, but the absolute error is down by about another factor of 10–20 because the overall amplitude of the density matrix goes down by about this much over the course of the time evolution. We also observe that the relative error is mainly a function of the barrier height, rather than N_b, the number of points in the PML.

3.5 Discussion and further directions

The density matrix formulation is a very natural way of approaching the time-evolution of open quantum systems. It is an efficient and numerically well-posed method of simulating the quantum mechanical density matrix, and it is the logical generalization of the work of Galdrikian and Birnir, discussed in Chapter 4, to open systems. Taking better account of the potential term in the PML procedure is still a work in progress. There may be some clues in the work of Ringhofer et al. [10]. But the method outlined here can already be extended in some useful directions:

Source terms In order to model the a system in contact with reservoirs, it is necessary to account for the information streaming into the computational domain as well as absorb the outgoing information. To address this, the total potential can be expressed as the sum of a time-independent part v_0 and a time-dependent part v_1, which is not necessarily small. Similarly, the total density matrix can be expressed as the sum of a stationary solution f_0 in the presence of v_0 only and the time-dependent fluctuations f_1 due to v_1. Then the total density matrix evolves according to

$$\partial_t(f_0 + f_1) = [i\partial_x\partial_\eta - i(\delta v_0 + \delta v_1)](f_0 + f_1). \tag{3.27}$$

Since f_0 is assumed to solve the Liouville-von Neumann equation in the presence of v_0 only, the expression above simplifies to

$$\partial_t f_1 = [i\partial_x\partial_\eta - i(\delta v_0 + \delta v_1)]f_1 - i\delta v_1 f_0. \tag{3.28}$$

The time evolution of the fluctuations is given by the usual Liouville-von Neumann equation for f_1, plus a source term due to the background solution f_0. Taking $v_0 = 0$, the stationary density matrix is equal to an integral over plane-wave states

$$f_0 = \int dk\, F(k,\mu)\psi_k^*(x + \tfrac{1}{2}\eta)\psi_k(x - \tfrac{1}{2}\eta), \tag{3.29}$$

where $F(k,\mu)$ is the Fermi function and $\psi_k(x) \propto \exp(ikx)$. Once the source term due to v_1 is turned on, the system will begin to evolve in time. The accuracy of this approach can be verified by choosing v_1 to be a time-independent potential barrier, and then showing that over long times, the solution of the Liouville-von Neumann equation approaches the stationary state of the transmission reflection problem.

Scattering terms If scattering terms were included, then the long-range (large η) correlations of the density matrix could be damped to zero before reaching the top edge of the domain. Under these circumstances, the potential could be held constant over two sufficiently wide intervals next to the left and right edges of the computational domain. Then L_x could be made as large as desired compared with L_η. Fixing L_η, the computational complexity would scale as $O(N_x \log N_x)$. This approach will be very useful for simulating microstructures in the time-dependent Hartree framework discussed in Chapter 4. However, in this work we have only investigated the effectiveness of PMLs at capturing the ballistic limit, in order to obtain quantitative measurement of the performance of the PML.

In order to account for interactions with an external system, such as a thermal bath of acoustic phonons, scattering terms can be included. In the splitting scheme for the time step, the discrete Wigner representation of the density matrix $w(x, k, t)$ is already computed as an intermediary, and it provides a natural place to introduce scattering terms [11]. The scattering terms could be treated according to the Fermi golden rule [3], and included as an additional step of the first-order splitting scheme. For a one-dimensional system of electrons, we have

$$(\partial_t w(x,k,t))_{\text{coll}} = \frac{2\pi}{\hbar} \sum_{k' \in \Omega} |\langle k|U|k'\rangle|^2 \{w(x,k')[1-w(x,k)] - w(x,k)[1-w(x,k')]\} \tag{3.30}$$

$$= \frac{2\pi}{\hbar} \sum_{k' \in \Omega} |\langle k|U|k'\rangle|^2 \{w(x,k') - w(x,k)\} \tag{3.31}$$

where Ω is the computational Brillouin zone, and U is the scattering interaction term.

Chapter 4

High-frequency parameter dependence of nonlinear dynamical phenomena in GaAs/(Al,Ga)As superlattices

An enormous effort was made by many experimentalists and theorists to understand the basic properties of two-dimensional electron gases during the 1970s and '80s. The intersubband absorption peak was found to be blue-shifted and at higher doping densities, which was surprising, given that the bare intersubband energy spacings grow progressively smaller with increased doping density. Hence it was shown that the absorption peak did not correspond to single-particle intersubband transitions, but to the collective response of *all* the electrons occupying the quantum well. This effect was termed the *depolarization shift*. It was also shown that the time-dependent Hartree approximation provided a reasonably quantitative model of the intersubband absorption of electromagnetic radiation. The level of agreement between the Hartree theory and the experimental

observations is quite remarkable, considering the simplicity of the theory [14].

In the 1990s, Bryan Galdrikian, a student of Mark Sherwin and also of Björn Birnir, of the Mathematics department and the Center for Complex and Nonlinear Science at UC Santa Barbara, simulated the nonlinear, time-dependent, self-consistent response of a 2DEG to a spatially uniform, out-of-plane-polarized electric field. For small external fields, this approach gives identical results to those of Ando et. al., who first calculated the self-consistent response in the Hartree (random-phase) approximation [15]. Galdrikian rigorously showed the mathematical equivalence of his approach to that of Ando et al. [16]. This intuitively-appealing approach can be described shortly as follows: The electronic density matrix evolves in time under the influence of a periodic external electric field. The time-dependent Hartree potential accounts for the the electron-electron interaction. The Hartree potential is computed according to an iterative procedure. Initializing it to zero, the following steps are performed:

1. The density matrix is evolved in time under the driving field until it settles onto a periodic orbit.

2. The time-dependent Hartree potential is computed from the periodic response of the density matrix by solving Poisson's equation.

3. The Hartree potential is added to the external field

4. Repeat the process above until the Hartree potential converges to the same time-periodic function at the end of each iteration.

The time-periodic Hartree iteration of Galdrikian et al. also allows for periodic orbits having periods longer than that the driving period. In particular, this theory predicted a period-doubling bifurcation, followed by a period-doubling cascade to chaos, in quantum

wells with certain assymetric "steps" built into the bottom of the confinement potential [17].

Semiconductor superlattices (SSLs) are GaAs/AlGaAs heterostructures that can be thought of as a number of identical quantum wells layered one atop the other. In contrast to the TACIT sensor, electron transport in SSLs occurs by tunneling from one well to the next, ie. through the barriers. Since the 1990s, it has been observed experimentally that the electronic dynamics of SSLs feature nonlinear Gunn-like oscillations and chaos at low temperatures [18]. More recently, and more surprisingly, similar nonlinear oscillations have been observed in SSLs at room temperature [39, 40]. A schematic diagram of the SSL developed by Huang et al. is shown in Figure 4.1.

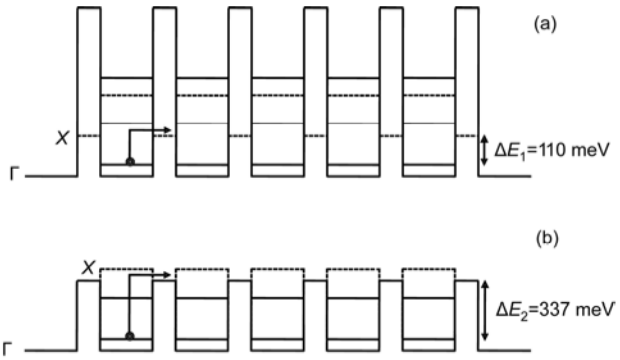

Figure 4.1: Schematic diagram of the conduction band in GaAs/AlGaAs superlattices, showing the energies of the Γ and X valleys, after Huang et al. [39]. The top image (a) corresponds to GaAs/$Al_{0.7}Ga_{0.3}$As SSLs and the bottom image corresponds to GaAs/$Al_{0.45}Ga_{0.55}$As SSLs.

In this work we will consider SSLs in the weakly-coupled, sequential tunneling limit. In this limit, the rate of tunneling transport is taken to occur on much longer timescales than the inter-subband transitions, and consequently the inter-subband processes are averaged away, replacing the populations of the subbands of each quantum well with thermal distributions, which depend on the sheet density. The tunneling only occurs when the quantized energy levels of adjacent wells are in alignment with an occupied level.

Similarly to the depolarization shift theory in single quantum wells, the nonlinearity in this model again comes from the response of the self-consistent potential to the shifting populations of the wells. It is worth mentioning that the recent observations of chaos in SSLs at room temperature were motivated by the idea of preserving the sequential tunneling limit at warmer temperatures.

This simple, self-consistent model of the time-evolution of the electric fields in SSLs, due to Luis Bonilla et al. [32] has also been shown to undergo period-doubling bifurcations and it also features a period-doubling cascade to chaos [34]. There is an interesting analogy to make between these results and those of Galdrikian et al. At face value, the theories appear to be quite different from one another, however it is our point of view that the nonlinearities and chaos induced by the Coulomb interaction in doped semiconductors can be very robust and apply equally well to both semiclassical and highly-quantized systems.

The sequential resonant tunneling (SRT) model of Bonilla et. al. (see reviews in [42, 37]) captures the essential physics of tunneling transport in SSLs. The model contains nonlinearities arising from feedback between resonant tunneling through the barriers and the self-consistent electric field of the mobile carriers. Simulations of the 50-period SSLs by Alvaro et. al. [33] demonstrated extreme sensitivity to weak stochastic perturbations of the local electric fields and the bias voltage, which provided a qualitative description of the experimental results. However, the unperturbed dynamics of the 50-period SRT model contained only a period doubling bifurcation, rather than fully-developed chaos. Recently, it was observed that shorter (10-period) SSLs, support chaotic oscillations on much faster timescales [34]. In contrast with the 50-period simulations, the chaos in shorter SSLs exhibited a complete period-doubling cascade.

One of the practical applications of chaotic oscillations in SSLs is the secure generation of random bit sequences. With faster chaotic oscillations, shorter SSLs would achieve

a higher random bit rate. In this work, we provide aid to the experimental search for period-doubling cascades in shorter SSLs by mapping out the response of the SRT model to variations of the basic design parameters.

We simulate the SRT theory, which describes electronic transport in SSLs in the weakly-coupled, self-consistent regime. Two different time scales are taken into account in this description: The inter-site tunneling and inter-subband relaxation processes occur on much shorter timescales than the dielectric relaxation processes [43]. Therefore, the long timescale dynamics of semiconductor lasers [30] and superlattices [32, 33] are typically modeled using semiclassical equations, while the short timescale processes are treated through the addition of stochastic terms to the dynamical equations. Nonlinearities enter the model via the the self-consistent electron-electron Coulomb interaction, which bends the conduction band of the SSL, modifying the inter-subband tunneling rates by casting the energy levels of adjacent wells into or out of resonance [43].

Over some intervals of the bias voltage, the total current $J(t)$ through the SSL is a monotonically increasing function of the bias voltage. At higher bias voltages, $J(t)$ suddenly changes to a time-dependent, oscillatory function, which undergoes a series of transitions, leading to chaotic behavior. We summarize the behavior of $J(t)$ below:

Bistability: The earliest signal of the oscillatory behavior is a bistable response of $J(t)$ to slow variations in V_{bias}. This behavior is observable only at sufficiently low temperatures [49, 50, 38]. Generically, bistable behavior is found at voltages just below those of the Hopf bifurcation described next.

Supercritical Hopf Bifurcation: As the bias voltage is increased, $J(t)$ undergoes a supercritical Hopf bifurcation. The fixed point becomes unstable, and $J(t)$ becomes attracted to a closed periodic orbit. In this regime, the SSL acts as a GHz oscillator

with a discrete power spectrum involving the frequencies $f_n = n/T,\ n = 1, 2, 3, ...$, where the *fundamental period* T is the period of the lowest-frequency oscillation present. The superharmonics $n > 1$ arise due to the nonlinearities of the SRT model. Since T varies smoothly with the bias voltage, the oscillator is also *tunable*.

Period Doubling Bifurcation: The periodic orbit described above is topologically equivalent to a circle in phase space. The Poincaré map of this trajectory consists of a single point, called a *one-cycle*. Increasing the bias voltage further, one-cycles of the Poincaré map transition to two-cycles, i.e. two points, meaning that the orbit circles twice before it closes onto itself. The fundamental period of the oscillator is doubled, $T \to 2T$, and the fundamental frequency is cut in half: $f_1 \to f_1/2$. A new peak appears in the power spectrum spectrum at half the fundamental frequency, and the number of superharmonics doubles. Following a period doubling bifurcation, it is possible that the reverse (period-halving) bifurcation may occur. We refer to the regions between these bifurcations as *period doubling bubbles*. An application of period doubling, due to the subharmonic peak, is the generation of *squeezed states* [47], which have applications in the area of noise reduction.

Period Doubling Cascade: An infinite number of period doublings is possible within a finite voltage interval. The invariant phase space structures transition from a smooth compact manifolds (periodic orbits of high periods) to irregular sets called *strange attractors*. The Poincaré map takes on a fractal structure.

Transport in SSLs can take place through two possible channels: Quantum tunneling between the Γ valleys of adjacent wells, or phonon-assisted transport through the X valley of the barriers (Γ-X transfer). Chaotic oscillations in SSLs are only possible when tunneling transport dominates over diffusive transport [39, 40]. The phonon-assisted

transport may be suppressed by (a) lowering the temperature of the SSL, (b) reducing the level of doping (and hence the Fermi energy), or (c) adding Aluminum to the barriers. For GaAs/AlAs SSLs, the X-valley of the AlAs barriers is only 110 meV higher than the lowest subband of the 4 nm GaAs wells considered in this paper. Adding Aluminum to the barriers has the effect of lowering the Γ-minimum and increasing the X-minimum. For $Al_xGa_{1-x}As$ SSLs with Aluminum concentration $x = 0.45$, the Γ- and X-minima are both 337meV above the lowest subband of the GaAs well. Therefore at room temperature, the $x = 0.45$ SSLs suppress the phonon-assisted transport by a factor of about 1.6×10^{-4} compared with the $x = 0$ SSLs [39]. In this work, we fix the doping density to $N_D = 6 \times 10^{10}$ cm^{-2} and simulate two scenarios: $GaAs/Al_{0.7}Ga_{0.3}As$ SSLs at 77K and $GaAs/Al_{0.45}Ga_{0.55}As$ SSLs at 295K.

With an eye towards development of fast, electronic true random number generators, we investigate the response of the chaotic signal to variations of the design parameters of these systems: The number of periods, the contact conductivity, and the strength of the *disorder* (aperiodicity) of the SSL. The outline of our paper is as follows: In Section 4.1, we review the SRT model. In Section 4.2, we describe the numerical methods. In Section 4.3, we present the results of our simulations. A discussion of our results is given in Section 4.4.

4.1 Model

Many phenomena are captured by SRT model of nonlinear charge transport in SSLs [32, 41, 42, 37]. Consider a weakly coupled superlattice having N identical periods of length l and total length $L = Nl$ subject to a dc bias voltage V_{bias}. The time evolution of the average electric field of SSL period i, F_i, and the total current density, $J(t)$, are

coupled together by Ampere's law

$$J(t) = \epsilon \frac{dF_i}{dt} + J_{i \to i+1}, \tag{4.1}$$

with the voltage bias constraint

$$\sum_{i=1}^{N} F_i = \frac{V_{\text{bias}}}{l}. \tag{4.2}$$

Fluctuations of F_i away from its average value $F_{\text{avg}} = eV_{\text{bias}}/L$ arise from the inter-site tunneling current $J_{i \to i+1}$, which appears in equation (4.1). A microscopic derivation of $J_{i \to i+1}$ produces the result [43, 41]

$$J_{i \to i+1} = \frac{en_i}{l} v^{(f)}(F_i) - J^{-}_{i \to i+1}(F_i, n_{i+1}, T), \tag{4.3}$$

in which n_i is the electron sheet density at site i, $-e < 0$ is the electron charge and T is the lattice temperature. The forward velocity, $v^{(f)}(F_i)$, which is modeled as a Lorentzian distribution, is peaked at resonant values of F_i, where the lowest energy level at site i are aligned with one of the levels at site $i+1$. The backward tunneling current is given by

$$J^{-}_{i \to i+1}(F_i, n_{i+1}, T) = \frac{em^* k_B T}{\pi \hbar^2 l} v^{(f)}(F_i) \ln \left[1 + e^{-\frac{eF_i l}{k_B T}} \left(e^{\frac{\pi \hbar^2 n_{i+1}}{m^* k_B T}} - 1 \right) \right], \tag{4.4}$$

where the reference value of the effective electron mass in $Al_xGa_{1-x}As$ is $m^* = (0.063 + 0.083x)m_e$, and k_B is the Boltzmann constant. The n_i are determined self-consistently from the discrete Poisson equation,

$$n_i = N_D + \frac{\epsilon}{e}(F_i - F_{i-1}), \tag{4.5}$$

N_D (cm^{-2})	d (nm)	w (nm)	s (μm)
6×10^{10}	4	7	60

V_{barr} (meV)	T (K)	E_1 (meV)	E_2 (meV)	E_3 (meV)
600	77	53	207	440
388	295	45	173	346

Table 4.1: (Top) The design parameters of the superlattice. (Bottom) Values of the potential barrier and energy levels for GaAs/$\mathrm{Al}_{0.7}\mathrm{Ga}_{0.3}$As and GaAs/$\mathrm{Al}_{0.45}\mathrm{Ga}_{0.55}$As superlattices, first and second row, respectively.

where N_D is the doping sheet density and ϵ is the average permittivity. The field variables F_i are constrained by boundary conditions at $i = 0$ and $i = N$ that represent Ohmic contacts with the electrical leads

$$J_{0\to 1} = \sigma_0 F_0, \quad J_{N\to N+1} = \sigma_0 \frac{n_N}{N_D} F_N, \tag{4.6}$$

where σ_0 is the contact conductivity. Shot and thermal noise can be added as indicated in [33, 44].

Table 4.1 gives the numerical values of the parameters used in the simulations. The GaAs/$\mathrm{Al}_{0.45}\mathrm{Ga}_{0.55}$As configuration corresponds with the configuration used in recent experiments [31, 39, 45]. The rest of the parameters are as follows: $A = s^2$ is the transversal area of the superlattice, d and w are the barrier and well widths, and $l = d + w$ is the SSL period. The contact conductivity σ_0 is a linear approximation of the behavior of $J_{0\to 1}$, which depends on the structure of the emitter. We treat σ_0 as an empirical parameter and investigate the response of the SRT model as it is varied. Some representative values have been chosen in order to reproduce the experimental results produced by Huang *et al.* with $N = 50$: $\sigma_0 = 0.783$ A/Vm for $V_{barr} = 388$ meV ($x = 0.45$) and $\sigma_0 = 0.06$ A/Vm for $V_{barr} = 600$ meV ($x = 0.7$), where V_{barr} is the height of the barrier [33, 39].

4.1.1 Noise

To model the unavoidable fluctuations in the bias voltage, as well as the short-timescale processes in the electronic dynamics, stochastic terms [33] are introduced into equations (4.1)–(4.6). To account for the noise in the bias voltage, equation (4.2) is modified to

$$\sum_{i=1}^{N} F_i = \frac{V_{\text{bias}} + \eta(t)}{l}, \tag{4.7}$$

where $\eta(t)$ is taken to be a Gaussian random variable with standard deviation σ_η. To account for the short-timescale processes at each site of the SSL, equation (4.1) is modified to include *shot noise* in the local tunneling current

$$\epsilon \frac{dF_i}{dt} + J_{i\to i+1}(F_i) + \xi_i(t) = J(t), \tag{4.8}$$

where

$$\langle \xi_i(t)\xi_j(t')\rangle = \frac{e}{A}\left[\frac{ev^{(f)}(F_i)}{l} n_i + J^{-}_{i\to i+1}(F_i, n_{i+1}, T) + 2J^{-}_{i\to i+1}(F_i, n_i, T)\right]\delta_{ij}\delta(t-t'). \tag{4.9}$$

We see that $\eta(t)$ is independent of i, while $\xi_i(t)$ are independent Gaussian random variables associated with each site of the SSL. The strength of the fluctuations in the bias voltage may be tuned via the empirical parameter σ_η, while the strength of the fluctuations in the local tunneling current is completely determined by the parameters of Table 4.1.

4.1.2 Disorder

We also consider time-independent perturbations that break the periodicity of the SSL. We introduce variations in the widths of the wells and barriers via the scaling parameters β_i and ζ_i. The perturbed well and barrier lengths are

$$w_i = \beta_i w, \tag{4.10}$$

$$d_i = \zeta_i d. \tag{4.11}$$

The change in total length of the SSL modifies the bias constraint equation (4.2) to

$$V_{\text{bias}} = \sum_{i=1}^{N} F_i l_i. \tag{4.12}$$

To lowest order, the energy levels scale with β_i according to

$$\varepsilon_i^{C,m} = \frac{\varepsilon^{C,m}}{\beta_i^2}. \tag{4.13}$$

These modifications imply that the effective dielectric constant becomes dependent on i,

$$\varepsilon_i = l_i/(w_i/\varepsilon_w + d_i/\varepsilon_d). \tag{4.14}$$

Following Bonilla et. al. [49], equations (4.3) and (4.4) are modified to account for the effects of disorder on $v^{(f)}(F_i)$ and τ_i:

$$v^{(f)}(F_i) = \frac{\hbar^3}{2m^{*2}} \sum_{m=1}^{3} \frac{l_i\Big(\gamma_{C1} + \gamma_{C,m}\Big)\tau_i(\varepsilon^i_{C,m})}{\Big(\varepsilon_i^{C,1} - \varepsilon_{i+1}^{C,m} + eF_i\Big(d_i + \frac{w_i+w_{i+1}}{2}\Big)\Big)^2 + \Big(\gamma_{C,1} + \gamma_{C,m}\Big)^2} \tag{4.15}$$

$$\tau_i = \frac{16k_i^2k_{i+1}^2\alpha_i^2}{\Big(k_i^2 + \alpha_i^2\Big)\Big(k_{i+1}^2 + \alpha_i^2\Big)\Big(w_i + \frac{1}{\alpha_{i-1}} + \frac{1}{\alpha_i}\Big)\Big(w_i + \frac{1}{\alpha_{i+1}} + \frac{1}{\alpha_i}\Big)e^{2\alpha_i d_i}} \tag{4.16}$$

The parameters $\gamma_{C,m}$ describe the width of the Lorentzian broadening functions that govern the degree to which the energy levels must be aligned in order for tunneling to take place. From reference [49], these are taken to be $\gamma_{C,1} = 2.5$ meV, $\gamma_{C,2} = 8.0$ meV, $\gamma_{C,3} = 24$ meV. The magnitudes of the propagating (k_i^m) or decaying (α_i^m) wavevectors are given by

$$\hbar k_i^m = \sqrt{2m^* \varepsilon_i^{C,m}} \tag{4.17}$$

$$\hbar k_{i+1}^m = \sqrt{2m^* \Big(\varepsilon_i^{C,m} + e \left[d_i + \frac{1}{2} \big(w_i + w_{i+1} \big) \right] F_i \Big)} \tag{4.18}$$

and

$$\hbar \alpha_{i-1}^m = \sqrt{2m^* \Big(eV_b + e \left[d_{i-1} + \frac{w_i}{2} \right] F_i - \varepsilon_i^{C,m} \Big)} \tag{4.19}$$

$$\hbar \alpha_i^m = \sqrt{2m^* \Big(eV_b - e \left[\frac{1}{2} w_i \right] F_i - \varepsilon_i^{C,m} \Big)} \tag{4.20}$$

$$\hbar \alpha_{i+1}^m = \sqrt{2m^* \Big(eV_b - e \left[d_i + \frac{1}{2} w_i + w_{i+1} \right] F_i - \varepsilon_i^{C,m} \Big)} \tag{4.21}$$

4.2 Computing the Poincaré map

The Poincaré map is used to gain insight into the structure of trajectories through high-dimensional space. In this section we outline our method of numerically computing the Poincaré map. The evolution equations (4.1)–(4.6) are evolved in time using the forward Euler method and the trajectory $(F_i(t), n_i(t), J(t))$ through the $(2N+1)$-dimensional phase space is stored. When applicable, the stochastic terms $\xi_i(t)$ and $\eta(t)$ are included using the Euler-Maruyama method. The first step is to construct the phase portrait, i.e. to project the evolution onto a two-dimensional surface in phase space. We choose the surface spanned by the the coordinates (F_i, F_j) for some values of i and

j near the anode and cathode of the SSL. Several phase portraits corresponding to a period-doubling cascade are illustrated in the second column of Figure 4.2.

The next step is to compute the Poincaré map of the phase portrait. After sufficient time has elapsed, and regardless of the initial conditions, the phase space trajectory settles onto one of the following time-invariant structures: (a) Fixed point, (b) periodic orbit, (c) strange attractor. The Poincaré map is used to distinguish between these structures. It is computed according to the following procedure: First, the transient behavior associated with the initial conditions is excised from the trajectory and only the remaining data is considered in what follows: When $F_i(t)$ passes through its median value, the time t^* and the field $F_j(t^*)$ are stored. We also compute the quantity $\dot{F}_i(t^*)$ from equation (4.1). We then discard all of the values of t^* for which $\dot{F}_i(t^*) > 0$, in order to prevent sampling the same orbit more than once per cycle. The remaining points constitute the Poincaré map $\mathcal{P}F_i$. The Poincaré map transforms the essentially continuous trajectory through phase space into a discrete map from the one-dimensional interval onto itself [46]. We represent it visually in terms of (a) phase portraits, plotting $\mathcal{P}F_j(t^*)$ against $\mathcal{P}\dot{F}_j(t^*)$, as in the third column of Figure 4.2, or (b) bifurcation diagrams, plotting $\mathcal{P}F_j$ against some external parameter such as the bias voltage, as in the bottom row of Figure 4.3.

Both fixed points and periodic orbits appear as a single point in the visualization of the Poincaré map. However, fixed points are easily distinguished from periodic orbits (one-cycles) by computing the power spectrum associated with the current $J(t)$:

$$P[J](f) = \left| \int_{t_i}^{t_f} dt\, e^{-i2\pi f t} J(t) \right|^2, \tag{4.22}$$

where f is the frequency. A period-doubling bifurcation is identified when one-cycles transition to two-cycles, producing two points in the Poincaré map. Chaotic regions are identified where a proliferation of period-doubling bifurcations occur, and the number of

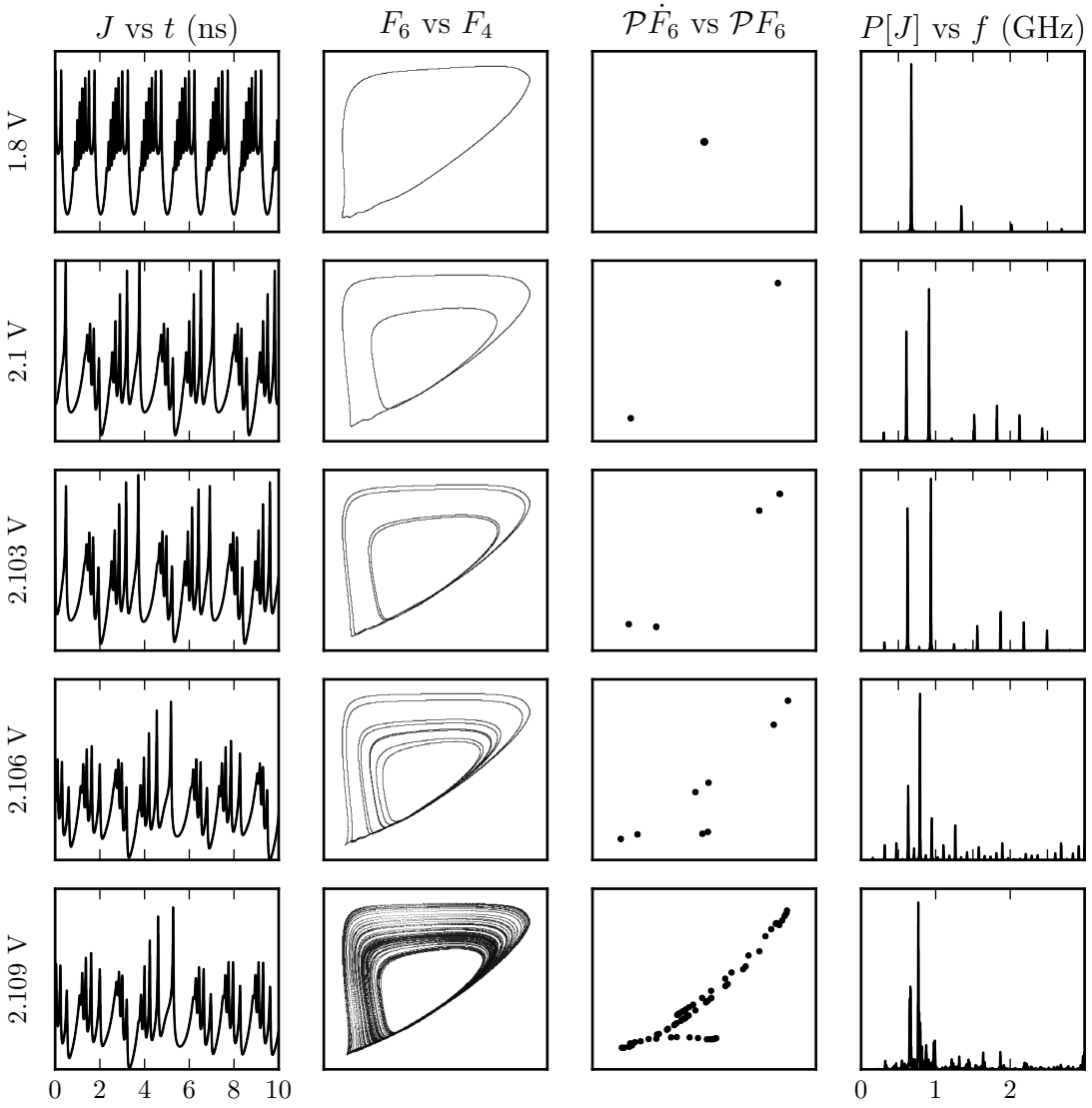

Figure 4.2: Representative phase portraits for the 10-period GaAs/$Al_{0.7}Ga_{0.3}As$ SSL. The first column shows the average current J plotted against time t. The second column shows the phase portrait $F_6(t)$ plotted against $F_4(t)$. The third column shows the Poincare map $\mathcal{P}\dot{F}_6(t^*)$ plotted against $\mathcal{P}F_6(t^*)$. The last column shows the power spectrum of $J(t)$. A periodic oscillation is shown in the first row. The period-doubling cascade to a chaotic attractor is shown in the bottom four rows. Reprinted figure with permission from M. Ruiz-Garcia et al., Phys. Rev. B 95, 085204 (2017). Copyright (2017) by the American Physical Society.

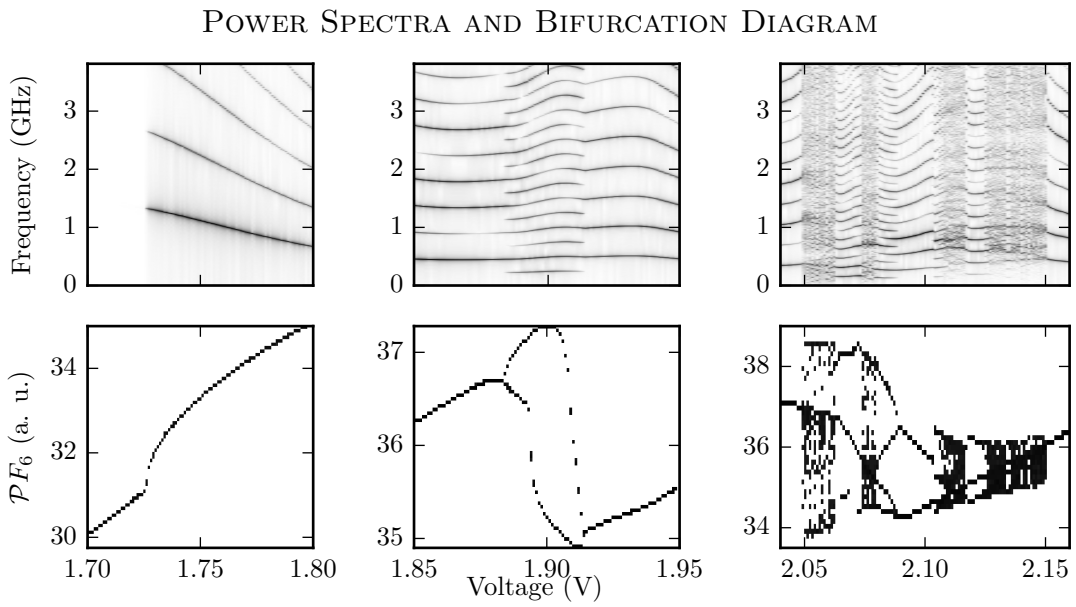

Figure 4.3: Power spectra and bifurcation diagram of a 10-period GaAs/$Al_{0.7}Ga_{0.3}As$ SSL. (Top row) Power spectrum of $J(t)$ versus voltage. (Bottom row) Bifurcation diagram of Poincaré map versus voltage. The Hopf bifurcation from the steady state is shown in the first column. A period doubling bubble is shown in the second column. A period-doubling cascade is shown in the third column. Reprinted figure with permission from M. Ruiz-Garcia et al., Phys. Rev. B 95, 085204 (2017). Copyright (2017) by the American Physical Society.

points in the Poincaré map increases without bound, yielding a fractal structure in the bifurcation diagram.

Dynamical structures revealed by the Poincaré map are associated with various power spectra as follows: (a) Periodic orbits correspond to a series of peaks with widths of the same order as the frequency bin size, falling at integer multiples of the fundamental frequency, (b) period doubling bifurcations are recognized when the number of peaks in the spectrum changes by a factor of two, and a new peak appears in the power spectrum at half the fundamental frequency, (c) chaotic attractors exhibit power spectra containing both sharp peaks and broadband noise. We illustrate the bifurcation diagram and power spectrum in Figure 4.3.

4.3 Results

Dynamical instabilities are found in two distinct *plateaus*, over which the local electric fields of the SSL cease to increase monotonically as a function of V_{bias}. The *first plateau* occurs at very low voltages, where tunneling transport between the ground states of adjacent wells are nearly aligned with one another in energy. The *second plateau* occurs in the region of V_{bias} such that the external electric field tilts the potential of the SSL to align the ground state of well i with first excited state of well $i+1$. We do not observe a third plateau because the third excited state becomes unbound at bias voltages that align it with the ground state of the previous well.

Within a plateau, we may observe period-doubling bifurcations, period-doubling cascades, and chaotic attractors, whose locations depend upon on the values of the rest of the parameters, in particular σ, the contact conductivity, N, the number of wells making up the SSL, and β (ζ), the strength of the perturbations to the well (barrier) widths. Shorter superlattices exhibit faster oscillations and a greater variety of dynamical behavior in the second plateau [34]. We are concerned with finding the parameter regions with the strongest nonlinear phenomena. Our observable of interest is the periodicity, i.e. the number of distinct points in the Poincaré map, which is equivalent to the number of branches in the bifurcation diagram. The nonlinear orbits of higher periodicity are found deeper into the period doubling cascade, either within or near to the chaotic windows.

An important empirical parameter of the SRT model is the contact conductivity. In Figure 4.4, we show the response of the periodicity to variations in the contact conductivity. We have chosen the values of N which maximize the total area of the high-period orbits in the Poincaré mapping as a function of voltage: $N = 14$ for GaAs/$Al_{0.7}Ga_{0.3}As$ SSLs, and $N = 10$ for GaAs/$Al_{0.45}Ga_{0.55}As$ SSLs.

In both cases we observe that the second plateau remains in existence for very low

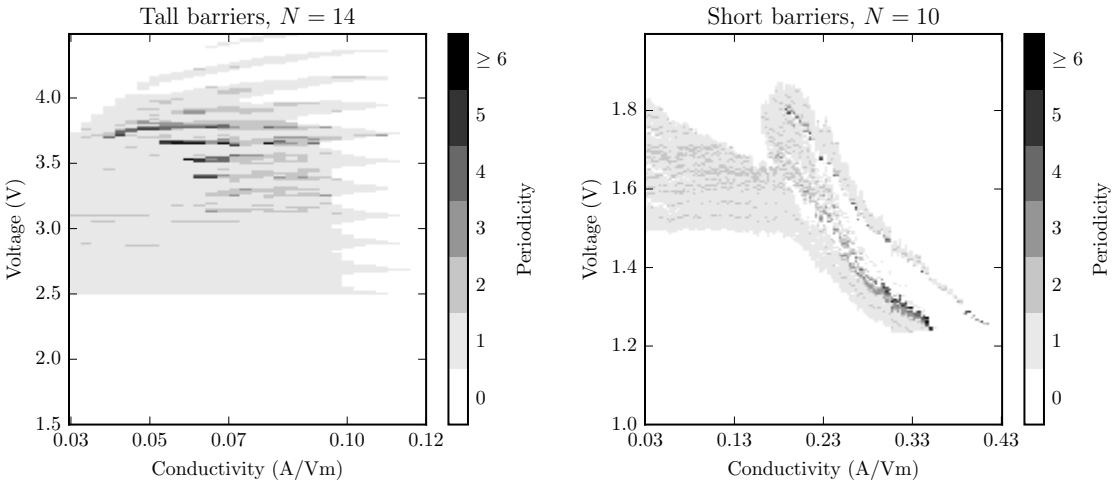

(a) GaAs/$Al_{0.7}Ga_{0.3}$As SSL (b) GaAs/$Al_{0.45}Ga_{0.55}$As SSL

Figure 4.4: Varying the conductivity. The second plateau is shown in the figures. It exists for low conductivities, then fragments and disappears for higher conductivity. The black dots and bands indicate orbits of high periodicity.

conductivity, then narrows, fragments, and disappears at sufficiently high conductivity. The highest-period orbits and chaos are concentrated at high conductivity and the highest voltages contained in the second plateau. These results suggest that in order to find the most chaotic dynamics, the highest possible conductivities that allow for the existence of the second plateau should be sought out. In the rest of our results, we set the conductivity to $\sigma = 0.06$ A/Vm for GaAs/$Al_{0.7}Ga_{0.3}$As SSLs (the same as in [34]) and $\sigma = 0.30$ V/Am for GaAs/$Al_{0.45}Ga_{0.55}$As SSLs.

We next consider varying N, the number of periods making up the SSL in Figure 4.5. In both cases, we observe a band of higher periodicity including chaotic behavior in the vicinity of $N = 10$. The shorter superlattice appears to have a gap in the chaotic behavior between N=10 and N=15, but in fact the voltage windows containing the chaos are too narrow to be observed at this scale. The band of chaotic behavior in the GaAs/$Al_{0.7}Ga_{0.3}$As SSLs is located along the higher voltages of the second plateau. In both cases, the chaotic windows narrow and finally close for values of N between 15 and

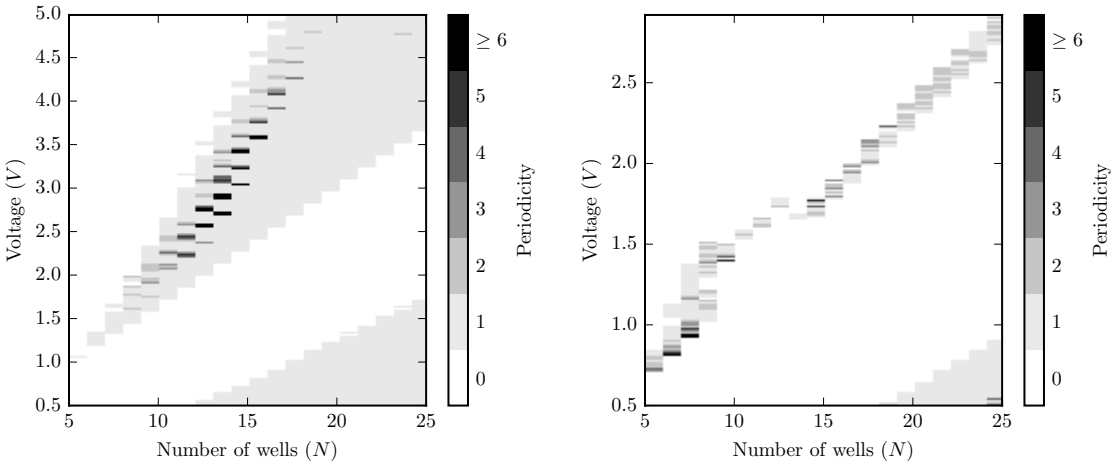

(a) GaAs/$Al_{0.7}Ga_{0.3}As$ SSL (b) GaAs/$Al_{0.45}Ga_{0.55}As$ SSL

Figure 4.5: Varying the number of wells N in the superlattice. A band of higher period orbits appears around $N = 10$, both for the tall barriers on the left and shorter barriers on the right. For the latter barriers the windows narrow to become hardly observable between $N = 11$ and $N = 14$.

20. Part of the first plateau is also visible in the bottom right corners of Figures 4.5b(a) and (b).

Finally, we investigate the sensitivity of the chaos to disorder by varying β in Figure 4.6. The width of one GaAs monolayer is about 0.28 nm. In our simulations, the addition of a single monolayer is capable of destroying the chaos in the case of the taller barriers. On the other hand, the chaotic signal of the shorter barriers appears to be enhanced by the presence of disorder. We note that the location of the added disorder is nearer to the cathode for the taller barriers and nearer to the anode for the shorter barriers. It would would be interesting to further investigate the conditions where the chaos is enhanced by the presence of disorder.

We simulate the effects of noise on the bifurcation diagram in Figure 4.7, including both shot noise and bias voltage noise. We can see that in regions where the periodicity (number of branches in the bifurcation diagram) is low, the noise widens the Poincaré

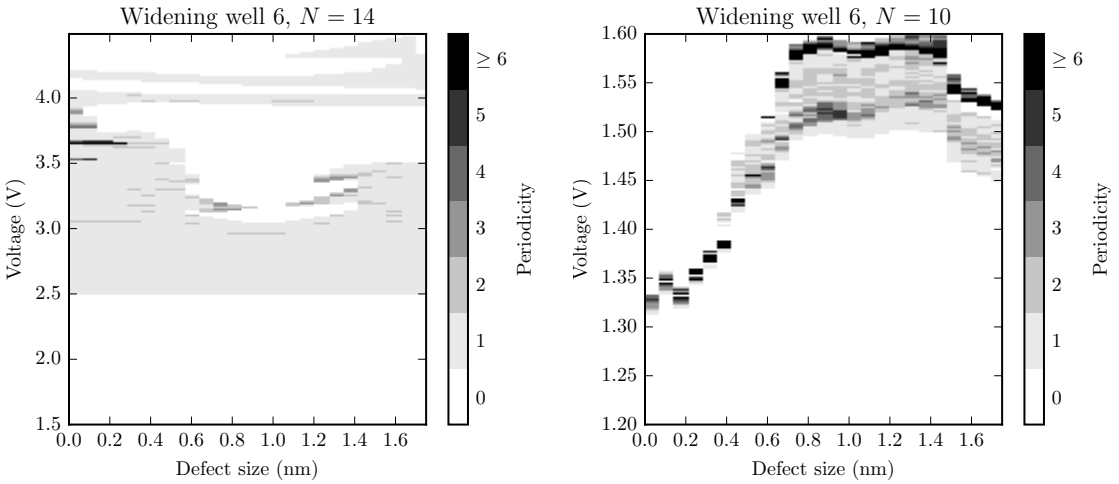

(a) GaAs/$Al_{0.7}Ga_{0.3}As$ SSL (b) GaAs/$Al_{0.45}Ga_{0.55}As$ SSL

Figure 4.6: Varying the disorder (defect size) β. (Left) the tall barriers permit high periodicity only for small values of β. (Right) the short barriers show greatly enhanced high periodicity at larger values of disorder ($\beta \geq 0.65$ nm).

map from an isolated point into a cluster, but the branches are still recognizable. On the other hand, where the periodicity is higher or the dynamics are chaotic, the noise widens the Poincaré map into a broad band.

Let us imagine an experiment which detects the local field F_6, shown in Figure 4.7, at some finite resolution, i.e. the number of bins, with the objective of reading out a sequence of random bits. Then the random bit generation rate will scale proportionally to the width of the Poincaré map times the resolution of the imaginary F_6-sensor. The bands within the regions of higher periodicity or intrinsic dynamical chaos would cover a larger number of bins. Hence these regions would generate random bits at higher bandwidth in comparison with the regions of lower periodicity. In practice, the local current I_6 would be easier to measure, but the results would be qualitatively very similar.

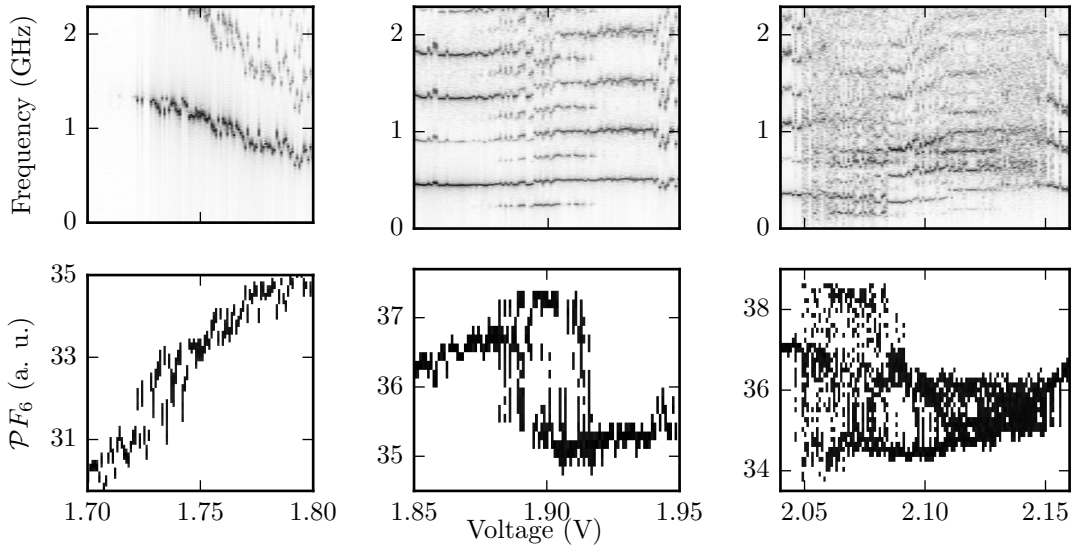

Figure 4.7: Including shot noise and bias noise for the N=10 GaAs/$Al_{0.7}Ga_{0.3}As$ SSL; the simulation parameters are otherwise the same as in Figure 4.3. The addition of noise widens the branches of the bifurcation diagram obscures the fine details of the period-doubling cascade.

4.4 Conclusions

The discovery of robust, high-frequency, intrinsic nonlinear phenomena and chaos in shorter semiconductor superlattices in the sequential tunneling regime points the way toward a variety of useful devices. In this work, we have characterized the response of the chaotic oscillations to variations in the number of SSL periods and the contact conductivity, providing a guide for the experimental investigation of the emergence of chaos in short SSLs. The chaos is predicted to appear as the result of a period-doubling cascade.

We have also investigated the response of the chaotic signal to stochastic perturbations in the local tunneling currents and the bias voltage. In contrast with the slower, noise-driven chaos in the first plateau for longer superlattices, we observe that shorter SSLs allow for faster, intrinsic chaos in the second plateau.

We have also investigated the effects of variations in the widths of the wells and

barriers on the period-doubling cascade. We find that the period-doubling cascade is very sensitive to these perturbations. An error of only a single monolayer has a strong impact on the width of the windows of chaotic behavior. The chaotic windows may be either widened or suppressed depending on the location of the irregularities, hence it may be possible to engineer aperiodicities in SSLs in order to increase the chaotic signal.

We had initially conjectured that the presence of aperiodicities could unfold the period-doubling bifurcation into a second Hopf bifurcation. However, this turned out not to be the case. Our study of the DC-biased SRT model shows only a period-doubling route to chaos (no second Hopf bifurcation). On the experimental side, quasi-periodic orbits and the associated invariant tori are commonplace. An interesting theoretical question is: By what mechanism do quasi-periodic orbits appear in weakly-coupled SSLs?

Appendix A

Transmission-reflection states

Figure A.1 shows the basic geometry of the transmission-reflection problem in one dimension. The active region is taken to be situated inside an infinitely-long channel in the x-direction. The interval $x \in [0, L_x]$ containing the active region is discretized into the N_x+1 points $x_j = jh_x$, where $j = 0 \ldots N_x$ and $h_x = L_x/N_x$. In the units of Appendix C.1 and the centered difference scheme, which has accuracy of $O(h_x^2)$, equation (1.10) is written on the interior of the active region as

$$-\frac{\psi_{j+1}^n + \psi_{j-1}^n - 2\psi_j^n}{2\Delta x^2} - \frac{1}{2}\sum_{n'}\left[2w_j^{nn'}\frac{\psi_{j+1}^{n'} - \psi_{j-1}^{n'}}{2\Delta x} + u_j^{nn'}\psi_j^{n'}\right] = \left[E_x - v_j - E_{zj}^n\right]\psi_j^n, \tag{A.1}$$

where $j = 1 \ldots J-1$. In order to impose the discrete transparent boundary condition below, we will assume that the contacts are completely flat in the x-direction: $v_1 = v_0$, $u_1^{nn'} = 0$, $w_1^{nn'} = 0$, and $E_{z1}^n = E_{z0}^n$. This implies a homogeneous Neumann boundary condition on the electrostatic potential.

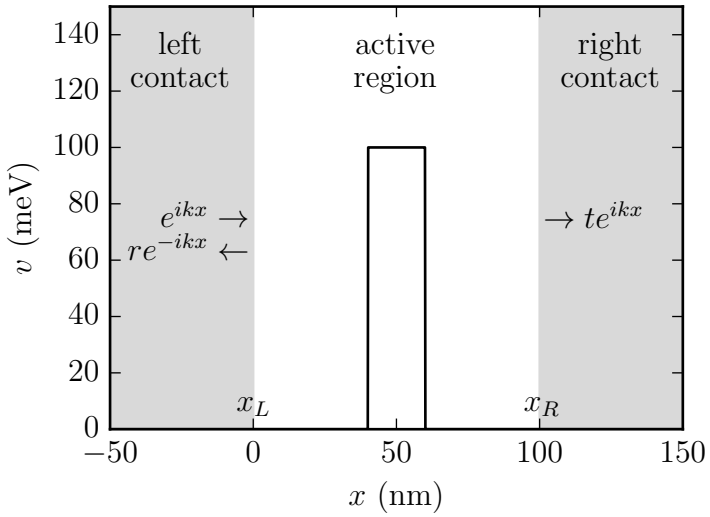

Figure A.1: Schematic diagram of the 1-dimensional transmission-reflection problem on a 100nm active region

Within the contacts, we have $w^{nn'} = 0$, $u^{nn'} = 0$,

$$\varepsilon^n(x) = \begin{cases} \varepsilon_0^n, & x \leq 0 \\ \varepsilon_J^n, & x \geq L \end{cases}$$

and

$$v(x) = \begin{cases} v_0, & x \leq 0 \\ v_J, & x \geq L \end{cases}$$

Then the discrete Schrödinger equation simplifies to

$$-\frac{1}{2}\frac{\psi_{j+1}^n + \psi_{j-1}^n - 2\psi_j^n}{\Delta x^2} = \left[E_x - v_j - \varepsilon^n\right]\psi_j^n$$

The solution in this case consists of left-and right-travelling plane waves.

Within the left contact,

$$\psi_j^n = (\sigma_\pm^n)^j, \quad j \leq 0$$

where

$$\sigma_{\pm}^{n} = 1 - (E_x - v_0 - \varepsilon_0^n)\Delta x^2 \pm i\sqrt{2(E_x - v_0 - \varepsilon_0^n)\Delta x^2 - (E_x - v_0 - \varepsilon_0^n)^2\Delta x^4}$$

Within the right contact,

$$\psi_j^n = (\tau_{\pm}^n)^j, \quad j \leq 0$$

where

$$\tau_{\pm}^{n} = 1 - (E_x - v_J - \varepsilon_J^n)\Delta x^2 \pm i\sqrt{2(E_x - v_J - \varepsilon_J^n)\Delta x^2 - (E_x - v_J - \varepsilon_J^n)^2\Delta x^4}$$

For a wave injected from the left, we need $\Delta x < \sqrt{2/(E_x - v_0 - \varepsilon_0^n)}$ in the left contact, in order that $(\sigma_{\pm}^n)^j$ be a traveling wave. Within the right contact, waves injected from the left may be either traveling or evanescent, depending on the sign of the discriminant. A similar condition on Δx holds for waves injected from the right contact.

The discrete momentum k^n of a left- or right-injected wave is defined by the relationship

$$\begin{cases} (E_x - v_0 - \varepsilon_0^n)\Delta x^2 = 1 - \cos k_0^n \Delta x, \quad k_0^n > 0 \quad \text{(left contact)} \\ (E_x - v_J - \varepsilon_J^n)\Delta x^2 = 1 - \cos k_J^n \Delta x, \quad k_J^n < 0 \quad \text{(right contact)} \end{cases}$$

Then we have

$$\begin{cases} \sigma_{\pm}^n = e^{\pm i k_0^n \Delta x}, \quad \text{(left contact)} \\ \tau_{\pm}^n = e^{\pm i k_J^n \Delta x}, \quad \text{(right contact)} \end{cases}$$

We will take

$$\Delta x < \min \begin{cases} \left\{\sqrt{2/(E_x - v_0 - \varepsilon_0^n)},\ \pi/k_0^n\right\} \\ \left\{\sqrt{2/(E_x - v_J - \varepsilon_J^n)},\ \pi/k_J^n\right\} \end{cases}$$

For a unit-amplitude wave injected from the left contact, the boundary condition at

the left contact is

$$\psi_j^n = (\sigma_+^n)^j + R(\sigma_+^n)^{-j}, \quad j \leq 1$$

where R is the reflection amplitude. Considering the $j = 0$ and $j = 1$ terms above and eliminating the R between them, the DTBC at the left contact is

$$-(\sigma_+^n)^{-1}\psi_0^n + \psi_1^n = \sigma_+^n - (\sigma_+^n)^{-1}$$

At the right contact,

$$\psi_j^n = T(\tau_+^n)^{j-J}, \quad j \geq J - 1$$

where T is the transmission amplitude. Considering the $j = J$ and $j = J - 1$ terms above and eliminating T between them, the DTBC at the right contact is

$$\psi_{J-1}^n - (\tau_+^n)^{-1}\psi_J^n = 0$$

Then the discrete Schrödinger equation for a unit-amplitude wave injected from the left into mode n is given in equation (A.2). The matrix on the lefthand side of the discrete stationary Schrödinger equation above is identical to G^{-1}, where G is the non-equilibrium Green function. The discrete transmission-reflection equation has a block-tridiagonal structure, which makes it considerably easier to solve.

$$
\begin{pmatrix}
\begin{pmatrix}
-(\sigma_+^0)^{-1} & & \\
& \ddots & \\
& & -(\sigma_+^N)^{-1}
\end{pmatrix}
\begin{pmatrix}
1 - \Delta x w_1^{00} & \cdots & -\Delta x w_1^{0N} \\
\vdots & \ddots & \vdots \\
-\Delta x w_1^{N0} & \cdots & 1 - \Delta x w_1^{NN}
\end{pmatrix} & \cdots & \begin{pmatrix}
1 & & \\
& \ddots & \\
& & 1
\end{pmatrix} \\
\vdots & \ddots & \\
\begin{pmatrix}
1 - \Delta x w_{J-1}^{00} & \cdots & -\Delta x w_{J-1}^{0N} \\
\vdots & \ddots & \vdots \\
-\Delta x w_{J-1}^{N0} & \cdots & 1 - \Delta x w_{J-1}^{NN}
\end{pmatrix} & & \begin{pmatrix}
-(\sigma_+^0)^{-1} & & \\
& \ddots & \\
& & -(\sigma_+^N)^{-1}
\end{pmatrix}
\end{pmatrix}
\begin{pmatrix}
\begin{pmatrix}
-2\left(1 - \Delta x^2\left[E_x - v_1 - \varepsilon_1^0\right]\right) + \Delta x^2 a_1^{00} & \cdots & \Delta x^2 a_1^{0N} \\
\vdots & \ddots & \vdots \\
\Delta x^2 a_1^{N0} & \cdots & -2\left(1 - \Delta x^2\left[E_x - v_1 - \varepsilon_1^N\right]\right) + \Delta x^2 a_1^{NN}
\end{pmatrix} & \cdots & \\
\vdots & \ddots & \\
\begin{pmatrix}
-2\left(1 - \Delta x^2\left[E_x - v_{J-1} - \varepsilon_{J-1}^0\right]\right) + \Delta x^2 a_{J-1}^{00} & \cdots & \Delta x^2 a_{J-1}^{0N} \\
\vdots & \ddots & \vdots \\
\Delta x^2 a_{J-1}^{N0} & \cdots & -2\left(1 - \Delta x^2\left[E_x - v_{J-1} - \varepsilon_{J-1}^N\right]\right) + \Delta x^2 a_{J-1}^{NN}
\end{pmatrix} & &
\end{pmatrix}
\begin{pmatrix}
\begin{pmatrix}
1 + \Delta x w_1^{00} & \cdots & \Delta x w_1^{0N} \\
\vdots & \ddots & \vdots \\
\Delta x w_1^{N0} & \cdots & 1 + \Delta x w_1^{NN}
\end{pmatrix} & \cdots & \\
\vdots & \ddots & \\
\begin{pmatrix}
1 + \Delta x w_{J-1}^{00} & \cdots & \Delta x w_{J-1}^{0N} \\
\vdots & \ddots & \vdots \\
\Delta x w_{J-1}^{N0} & \cdots & 1 + \Delta x w_{J-1}^{NN}
\end{pmatrix} & & \begin{pmatrix}
-(\sigma_+^0)^{-1} & & \\
& \ddots & \\
& & -(\sigma_+^N)^{-1}
\end{pmatrix}
\end{pmatrix}
\begin{pmatrix}
\begin{pmatrix}
\psi_0^0 \\ \vdots \\ \psi_0^N
\end{pmatrix} & \cdots & \begin{pmatrix}
\psi_1^0 \\ \vdots \\ \psi_1^N
\end{pmatrix} & \cdots & \\
\vdots & & \vdots & \ddots & \\
\begin{pmatrix}
\psi_{J-1}^0 \\ \vdots \\ \psi_{J-1}^N
\end{pmatrix} & \cdots & \begin{pmatrix}
\psi_J^0 \\ \vdots \\ \psi_J^N
\end{pmatrix} & &
\end{pmatrix}
=
\begin{pmatrix}
\begin{pmatrix}
0 \\ \vdots \\ \sigma_+^0 - (\sigma_+^0)^{-1}
\end{pmatrix} & \cdots & \begin{pmatrix}
0 \\ \vdots \\ 0
\end{pmatrix} & \cdots & \begin{pmatrix}
0 \\ \vdots \\ 0
\end{pmatrix} \\
\vdots & & \vdots & & \vdots \\
\begin{pmatrix}
0 \\ \vdots \\ 0
\end{pmatrix} & \cdots & \begin{pmatrix}
0 \\ \vdots \\ 0
\end{pmatrix} & \cdots & \begin{pmatrix}
0 \\ \vdots \\ 0
\end{pmatrix}
\end{pmatrix}
\tag{A.2}
$$

Appendix B

Numerical solution of Poisson's equation

Here we describe the numerical solution of Poisson's equation in 2d We start with the continuous Poisson equation

$$(\partial_x^2 + \partial_z^2)u(x,z) = f(x,z)$$

with mixed boundary conditions:

- Specify the electric field at the source and drain contacts, $x = 0, L_x$ (Neumann condition)
- Specify the electric potential along the top and bottom contacts, $z = 0, L_z$ (Dirichlet condition)

It is tempting to use the discrete sine transform (DST) along the Dirichlet direction and a discrete cosine transform (DCT) along the Neumann direction. However the purely spectral method only works properly for the pure Dirichlet problem. Placing a line of

constant charge between the source to the drain, the pure spectral method results in a potential function equal to zero. This is because the zero-frequency term in the basis of cosines must be neglected in order to invert the Laplacian operator, and DCT of a line of constant charge contains only the zero-frequency contribution.

Therefore, a hybrid approach has been implemented following some notes by William McLean of Northwestern University. The idea is to take only the DST, which results in a set of uncoupled tridiagonal equations in the mixed coordinate space, which may be solved with the Crout algorithm, in parallel.

Next, we make a finite difference approximation. Let $u_{ij} \approx u(x_i, z_j)$, and similar for $f(x, z)$, where

$$(x_i, z_j) = (ih_x, jh_z), \quad i = 0 \dots N_x, \quad j = 0 \dots N_z$$

Using the central difference scheme, the discrete Poisson equation is

$$\frac{u_{i+1,j} + u_{i-1,j} - 2u_{i,j}}{h_x^2} + \frac{u_{i,j+1} + u_{i,j-1} - 2u_{i,j}}{h_z^2} = f_{i,j}$$

Next, we take the DST in the z-direction. Let

$$u_{i,j} = \sum_{m=1}^{N_z - 1} \hat{u}_{i,m} \sin\left(\frac{\pi j m}{N_z}\right)$$

Making use of the identity

$$\sin(a + b) = \sin(a)\cos(b) + \cos(a)\sin(b)$$

we have

$$u_{i,j+1} = \sum_m \hat{u}_{i,m} \left[\sin\left(\frac{\pi j m}{N_z}\right)\cos\left(\frac{\pi m}{N_z}\right) + \cos\left(\frac{\pi j m}{N_z}\right)\sin\left(\frac{\pi m}{N_z}\right)\right]$$

$$u_{i,j-1} = \sum_m \hat{u}_{i,m} \left[\sin\left(\frac{\pi j m}{N_z}\right) \cos\left(\frac{\pi m}{N_z}\right) - \cos\left(\frac{\pi j m}{N_z}\right) \sin\left(\frac{\pi m}{N_z}\right) \right]$$

As a result, the second term in Poisson's equation simplifies considerably. After a few more steps, Poisson's equation becomes

$$\frac{\hat{u}_{i+1,m} + \hat{u}_{i-1,m} - 2\hat{u}_{i,m}}{h_x^2} + 2\left[\cos\left(\frac{\pi m}{N_z}\right) - 1\right] \frac{\hat{u}_{i,m}}{h_z^2} = \hat{f}_{i,m}$$

which is equivalent to

$$\frac{\hat{u}_{i+1,m} + \hat{u}_{i-1,m}}{h_x^2} + \left(\frac{2}{h_z^2}\left[\cos\frac{\pi m}{N_z} - 1\right] - \frac{2}{h_x^2} \right) \hat{u}_{i,m} = \hat{f}_{i,m}$$

In these mixed coordinates, Poisson's equation appears as a set of $N_z - 1$ uncoupled tridiagonal equations (one for each value of m). Each tridiagonal equation will involve $N_x + 1$ variables.

Next we need to address the boundary conditions. At $x = 0, L_x$ (source and drain contacts), we will have Neumann conditions.

$$\partial_x \, u(x,z)|_{x=0} = s(z)$$

$$\partial_x \, u(x,z)|_{x=L_x} = d(z)$$

We will impose these conditions using a centered difference scheme. Introducing 'ghost points,' labeled with a tilde, which represent the value of u just outside the computational domain, we have

$$\frac{u_{1,j} - \tilde{u}_{-1,j}}{2h_x} = s_j$$

$$\frac{\tilde{u}_{N_x+1,j} - u_{N_x-1,j}}{2h_x} = d_j$$

for $j = 1 \ldots N_z - 1$, The data at the ghost points is completely determined by the data

inside the computational domain

$$\tilde{u}_{-1,j} = u_{1,j} - 2h_x s_j$$

$$\tilde{u}_{N_x+1,j} = u_{N_x-1,j} + 2h_x d_j$$

Substituting into Poisson's equation at the boundaries, we have

$$\frac{2\hat{u}_{1,m}}{h_x^2} + \left(\frac{2}{h_z^2}\left[\cos\frac{\pi m}{N_z} - 1\right] - \frac{2}{h_x^2}\right)\hat{u}_{0,m} = \hat{f}_{0,m} + \frac{2}{h_x}\hat{s}_m$$

and

$$\frac{2\hat{u}_{N_x-1,m}}{h_x^2} + \left(\frac{2}{h_z^2}\left[\cos\frac{\pi m}{N_z} - 1\right] - \frac{2}{h_x^2}\right)\hat{u}_{N_x,m} = \hat{f}_{N_x,m} - \frac{2}{h_x}\hat{d}_m$$

We can see that the difference between the solution of the inhomogeneous problem and the homogeneous problem may be accounted for by a modification of the source term at the boundary.

$$f_{0,j} \to f_{0,j} + \frac{2}{h_x}s_j$$

$$f_{N_x,j} \to f_{N_x,j} - \frac{2}{h_x}d_j$$

At the boundaries at $z = 0, L_z$ (top and back gates) we will have Dirichlet conditions.

$$u(x,z)|_{z=0} = b(x)$$

$$u(x,z)|_{z=L_z} = t(x)$$

In discrete form, these conditions are

$$u_{i,0} = b_i$$

$$u_{i,N_x} = t_i$$

Similarly to before, the solution to the inhomogeneous problem may be obtained from the homogeneous problem with a modified source term.

$$f_{i,1} \to f_{i,1} - \frac{1}{h_z^2} b_i$$

$$f_{i,N_z-1} \to f_{i,N_z-1} - \frac{1}{h_z^2} t_i$$

A more detailed explanation may be found in Numerical Recipes ch 19.4 [6].

Appendix C

Some elementary results

These results are useful as a reference throughout the discussion of PMLs

C.1 Units

Start with Schrödinger's equation

$$i\hbar\partial_t\psi(x,t) = \left[-\frac{\hbar^2}{2m}\partial_x^2 + v(x)\right]\psi(x,t)$$

We choose the unit of energy $[E]$ to be

$$[E] = 1\text{meV}$$

and the unit of length $[x]$ such that the coefficient in front of the x-derivative term is equal to $1/2$

$$\frac{\hbar^2}{m[x]^2}\text{J}\cdot\frac{1\text{eV}}{1.6\cdot 10^{-19}\text{J}}\cdot\frac{1000\text{meV}}{1\text{eV}} = 1\text{meV},$$

where $m = m_e/15$ is the effective mass of the electron in GaAs. This gives the unit of length

$$[x] = 33.8\text{nm}$$

We choose the unit of time so that the coefficient in front of the t-derivative term is equal to i

$$\frac{\hbar}{[t]}\text{J} \cdot \frac{1\text{eV}}{1.6 \cdot 10^{-19}\text{J}} \cdot \frac{1000\text{meV}}{1\text{eV}} = 1\text{meV}$$

This gives the unit of time

$$[t] = 0.658\text{ps}$$

(notice that $1\text{ps} = 1\text{THz}^{-1}$).

C.2 Gaussian wave packets

In our unit system, with $v = 0$, Schrödinger's equation is

$$i\partial_t \psi(x,t) = -\tfrac{1}{2}\partial_x^2 \psi(x,t).$$

We can see that a traveling wave solution is

$$\xi_k(x,t) = e^{i\left(kx - \frac{1}{2}k^2 t\right)}.$$

We can write the general solution as

$$\psi(x,t) = \int \frac{dk}{2\pi} A(k)\xi_k(x,t).$$

Choosing

$$A(k) = \mathcal{N} e^{-\frac{1}{2}\sigma^2(k-k0)^2}$$

and doing the integral over k, we have

$$\psi(x,t) = \frac{\mathcal{N}}{\sqrt{2\pi}} \frac{1}{\sqrt{\sigma^2 - it}} \exp\left[-\frac{\frac{1}{2}x^2 + i\sigma^2(k_0 x - \frac{1}{2}k_0^2 t)}{\sigma^2 - it} \right]$$

With the normalization $1 = \int dx\, |\psi(x,t)|^2$, we have $\mathcal{N} = \sqrt{2\sigma\sqrt{\pi}}$.

C.3 Discretization of Schrödinger's equation in 1D

We begin with

$$i\partial_t \psi(x,t) = [-\tfrac{1}{2}\partial_x^2 + v(x)]\psi(x,t).$$

Discretizing the x-coordinate $x \to x_j$, where $x_j = jh_x$, and $j = 0 \ldots N_x$, with the central difference scheme, we have

$$i\partial_t \psi(x_j,t) = -\frac{1}{2h_x^2}[\psi(x_{j-1},t) + \psi(x_{j+1},t) - 2\psi(x_j,t)] + v(x_j)\psi(x_j,t) + \mathcal{O}(h_x^3).$$

We rewrite this in matrix form as

$$i\partial_t \vec{\psi}(t) = H\vec{\psi}(t),$$

where $\vec{\psi}(t) = (\psi(x_0,t),\ \ldots, \psi(x_{N_x},t))^\intercal$, and

$$[H]_{j,j'} = -\frac{1}{2h_x^2}(\delta_{j-1,j'} + \delta_{j+1,j'} - 2\delta_{j,j'}) + v(x_j)\delta_{j,j'}.$$

The boundary values of H are determined from the vanishing boundary condition

$$\psi(x_0,t) = \psi(x_{N_x},t) = 0.$$

Discretizing the t-coordinate $t \to t_s$, where $t_s = sh_t$, and $s = 0, 1, \ldots$, with the Crank-Nicolson scheme, we have

$$[1 - \tfrac{i}{2}h_t H]\vec{\psi}(t_{s+1}) = [1 + \tfrac{i}{2}h_t H]\vec{\psi}(t_s) \tag{C.1}$$

Bibliography

[1] G. B. Serapiglia, M. Hanson, M. F. Doty, P. Focardi, W. R. McGrath, A. C. Gossard, and M. S. Sherwin, *Ultrafast voltage-tunable detectors for Terahertz radiation operating above 100K*, *ArXiv e-prints* (Oct., 2014) [arXiv:1410.5019].

[2] A. Arnold, *Mathematical concepts of open quantum boundary conditions*, *Transport Theory and Statistical Physics* **30** (2001), no. 4-6 561–584.

[3] J. H. Davies, *The physics of low-dimensional semiconductors: an introduction*. Cambridge university press, 1997.

[4] N. Gautam, J. Kawamura, N. Chahat, B. Karasik, P. Focardi, S. Gulkis, L. Pfeiffer, and M. Sherwin, *Tunable antenna coupled intersubband terahertz detector*, in *2014 39th International Conference on Infrared, Millimeter, and Terahertz waves (IRMMW-THz)*, pp. 1–2, Sept, 2014.

[5] K. Duru and G. Kreiss, *Stable perfectly matched layers for the schrödinger equations*, in *Numerical Mathematics and Advanced Applications 2009*, pp. 287–295. Springer, 2010.

[6] W. H. Press, B. P. Flannery, S. A. Teukolsky, W. T. Vetterling, *et. al.*, *Numerical recipes*, vol. 3. cambridge University Press, cambridge, 1989.

[7] M. J. M. Lennan, *Quantum ballistic transport in semiconductor heterostructures*, Master's thesis, Perdue University, May, 1987.

[8] N. B. Abdallah and O. Pinaud, *Multiscale simulation of transport in an open quantum system: Resonances and WKB interpolation*, *Journal of Computational Physics* **213** (2006), no. 1 288–310.

[9] A. Arnold, *A mixed spectral-collocation and operator splitting method for the wigner-poisson equation*, in *Mathematics of Computation, 1943-1993: A Half-century of Computational Mathematics: Mathematics of Computation 50th Anniversary Symposium, August 9-13, 1993, Vancouver, British Columbia*, vol. 48, p. 249, American Mathematical Soc., 1994.

[10] C. Ringhofer, D. Ferry, and N. Kluksdahl, *Absorbing boundary conditions for the simulation of quantum transport phenomena*, *Transport Theory and Statistical Physics* **18** (June, 1989) 331–346.

[11] W. R. Frensley, *Boundary conditions for open quantum systems driven far from equilibrium*, *Rev. Mod. Phys.* **62** (Jul, 1990) 745–791.

[12] B. Eliasson, *Outflow boundary conditions for the fourier transformed one-dimensional vlasov–poisson system*, *Journal of Scientific Computing* **16** (2001), no. 1 1–28.

[13] L. L. Bonilla and S. W. Teitsworth, *Nonlinear wave methods for charge transport*. John Wiley & Sons, 2009.

[14] K. Craig, B. Galdrikian, J. Heyman, A. Markelz, J. Williams, M. Sherwin, K. Campman, P. Hopkins, and A. Gossard, *Undressing a collective intersubband excitation in a quantum well*, *Physical review letters* **76** (1996), no. 13 2382.

[15] T. Ando, A. B. Fowler, and F. Stern, *Electronic properties of two-dimensional systems*, *Reviews of Modern Physics* **54** (1982), no. 2 437.

[16] B. Galdrikian, *Nonlinear and nonperturbative dynamics in quantum wells*. PhD thesis, UC Santa Barbara, 1994.

[17] B. Galdrikian and B. Birnir, *Period doubling and strange attractors in quantum wells*, *Physical review letters* **76** (1996), no. 18 3308.

[18] K. J. Luo, H. T. Grahn, K. H. Ploog, and L. L. Bonilla, *Explosive bifurcation to chaos in weakly coupled semiconductor superlattices*, *Phys. Rev. Lett.* **81** (Aug, 1998) 1290–1293.

[19] D.R. Stinson, *Cryptography: Theory and Practice, 3rd ed.* (CRC Press, Boca Raton, 2006).

[20] R.G. Gallager, *Principles of Digital Communication* (Cambridge University Press, Cambridge, UK, 2008).

[21] M.A. Nielsen, I.L. Chuang, *Quantum Computation and Quantum Information* (Cambridge University Press, Cambridge, UK, 2000).

[22] S. Asmussen, P.W. Glynn, *Stochastic Simulation: Algorithms and Analysis* (Springer-Verlag, New York, 2007).

[23] Karl Leo and Peter Haring Bolivar and Frank Brüggemann and Ralf Schwedler and Klaus Köhler. Observation of Bloch oscillations in a semiconductor superlattice. Solid State Communications **10**, 943–946 (1992).

[24] Kastrup, J and Hey, R and Ploog, KH and Grahn, HT and Bonilla, LL and Kindelan, M and Moscoso, M and Wacker, A and Galán, J. Electrically tunable GHz oscillations in doped GaAs-AlAs superlattices. Phys Rev B. **55**, 2476 (1997).

[25] Wu, JQ and Jiang, DS and Sun, BQ. Room-temperature microwave oscillation in AlAs/GaAs superlattices. Physica E: Low-dimensional Systems and Nanostructures, 137–141 (1999).

[26] A. Uchida, K. Amano, M. Inoue, K. Hirano, S. Naito, H. Someya, I. Oowada, T. Kurashige, M. Shiki, S. Yoshimori, K. Yoshimura, P. Davis, Fast physical random bit generation with chaotic semiconductor lasers. Nat. Photonics **2**, 728-732 (2008).

[27] T. E. Murphy and R. Roy, The world's fastest dice. Nat Photonics. **2**, 714-715 (2008)

[28] I. Reidler, Y. Aviad, M. Rosenbluh, I. Kanter, Ultrahigh-speed random number generation based on a chaotic semiconductor laser. Phys Rev Lett. **103**, 024102 (2009)

[29] I. Kanter, Y. Aviad, I. Reidler, E. Cohen, M. Rosenbluth. An optical ultrafast random bit generator. Nat Photonics. **4**, 58 (2010).

[30] M. Sciamanna, K.A. Shore, Physics and applications of laser diode chaos. Nature Photonics **9**, 151-162 (2015).

[31] W. Li, I. Reidler, Y. Aviad, Y. Y. Huang, H. Song, Y. H. Zhang, M. Rosenbluh, and I. Kanter, Fast Physical Random-Number Generation Based on Room-Temperature Chaotic Oscillations in Weakly Coupled Superlattices, Phys. Rev. Lett. **111**, 044102 (2013)

[32] L. L. Bonilla and H. T. Grahn, Non-linear dynamics of semiconductor superlattices. Reports on Progress in Physics **68**, 577 (2005)

[33] M. Alvaro, M. Carretero, and L. Bonilla, Noise-enhanced spontaneous chaos in semiconductor superlattices at room temperature. EPL (Europhysics Letters) **107**, 37002 (2014)

[34] Ruiz-Garcia, M. and Essen, J. and Carretero, M. and Bonilla, L. L. and Birnir, B., Enhancing chaotic behavior at room temperature in GaAs/(Al,Ga)As superlattices, Phys. Rev. B **95**, 085204 (2017).

[35] B. Galdrikian and B. Birnir, Period Doubling and Strange Attractors in Quantum Wells. Phys. Rev. Lett. **76**, 3308 (1996)

[36] A. A. Batista, B. Birnir, P. I. Tamborenea and D. S. Citrin, Period-doubling and Hopf bifurcations in far-infrared driven quantum well intersubband transitions. Phys. Rev. B **68**, 035307 (2003)

[37] A. Amann, J. Schlesner, A. Wacker, E. Schöll, Chaotic front dynamics in semiconductor superlattices. Phys. Rev. B **65**, 193313 (2002).

[38] Luo K J, Teitsworth S W, Kostial H, Grahn H T and Ohtani N, Controllable bistabilities and bifurcations in a photoexcited GaAs/AlAs superlattice. Appl. Phys. Lett. **74** 3845 (1999)

[39] Y. Huang, W. Li, W. Ma, H. Qin, and Y. Zhang, Experimental observation of spontaneous chaotic current oscillations in GaAs/Al0.45Ga0.55As superlattices at room temperature. Chinese Science Bulletin **57**, 2070 (2012)

[40] Y. Huang, W. Li, W. Ma, H. Qin, H. T. Grahn, and Y. Zhang, Spontaneous quasi-periodic current self-oscillations in a weakly coupled GaAs/(Al,Ga)As superlattice at room temperature. Applied Physics Letters **102**, 242107 (2013)

[41] L. L. Bonilla, Theory of Nonlinear Charge Transport, Wave Propagation and Self-oscillations in Semiconductor Superlattices. Journal of Physics: Condensed Matter **14**, R341 (2002)

[42] L. L. Bonilla and S. W. Teitsworth, *Nonlinear wave methods for charge transport.* (Wiley VCH, Weinheim, 2009)

[43] L. L. Bonilla, G. Platero, and D. Sánchez, Microscopic derivation of transport coefficients and boundary conditions in discrete drift-diffusion models of weakly coupled superlattices. Phys. Rev. B **62**, 2786 (2000)

[44] L.L. Bonilla, M. Alvaro, and M. Carretero, Chaos-based true random number generators. Journal of Mathematics in Industry **7**, 1 (2016).

[45] Z. Yin, Y. Zhang, M. Ruiz-García, M. Carretero, L. L. Bonilla, K. Biermann and H. T. Grahn, Noise-enhanced chaos in a weakly coupled GaAs/(Al,Ga)As superlattice, unpublished.

[46] P. Collet and J. Eckmann, *Iterated Maps on the Interval as Dynamical Systems*, Modern Birkhäuser Classics (Birkhäuser Boston, 2009).

[47] R. Graham, Squeezing and frequency changes in harmonic oscillations. Journal of Modern Optics **34**, 873 (1987)

[48] A. A. Batista, P. I. Tamborenea, B. Birnir, M. Sherwin, and D. S. Citrin, Nonlinear dynamics in far-infrared driven quantum-well intersubband transitions. Phys. Rev. B **66**, 195325 (2002)

[49] L. L. Bonilla, R. Escobedo, and G. Dell'Acqua, Voltage switching and domain relocation in semiconductor superlattices. Phys. Rev. B **73**, 115341 (2006)

[50] G. Dell'Acqua, L. L. Bonilla, and R. Escobedo, Hopf Bifurcation in a Superlattice Model, Proceedings of the International Conference on Computational and Mathematical Methods in Science and Engineering (2006).